



## Decadal changes of anthropogenic carbon in the Atlantic 1990–2010

Reiner Steinfeldt<sup>1</sup>, Monika Rhein<sup>2</sup>, and Dagmar Kieke<sup>1,2,3</sup>

<sup>1</sup>Institute of Environmental Physics, University of Bremen, Bremen, Germany

<sup>2</sup>MARUM - Center for Marine Environmental Sciences, University of Bremen, Bremen, Germany

<sup>3</sup>now at Federal Maritime and Hydrographic Agency (BSH), Hamburg, Germany

**Correspondence:** Reiner Steinfeldt (rsteinf@physik.uni-bremen.de)

**Abstract.** The Atlantic inventory of anthropogenic carbon ( $C_{\text{ant}}$ ) and its changes between 1990 and 2010 are investigated by applying the transit time distribution (TTD) method to anthropogenic tracer data. In contrast to previous TTD applications, here we take into account the admixture of old waters free of anthropogenic tracers. The greatest difference to other methods based on direct carbon observations is the higher  $C_{\text{ant}}$  storage in the deep ocean. The results from the TTD method better reflects the observed distribution of other transient tracers such as chlorofluorocarbons (CFCs). Changes in oceanic circulation/ventilation are important on the regional scale. The enhanced upwelling of older water in the Southern Ocean and the decline in the convection depth in the Labrador Sea lead to deviations of the inferred  $C_{\text{ant}}$  increase between 1990 and 2010 from the rate equivalent to a steady state ocean. For the total Atlantic  $C_{\text{ant}}$  inventory, however, decadal ventilation variability of individual water masses is partially compensating each other, and the effect is small due to the much higher flushing time for the total Atlantic of the order of hundreds of years. The total  $C_{\text{ant}}$  inventory increases from  $39.7 \pm 7.7 \text{Pg C}$  in 1990 to  $54.6 \pm 9.5 \text{Pg C}$  in 2010, almost in unison with the rising  $\text{CO}_2$  in the atmosphere. Only a reduction of the Atlantic ventilation over several decades would severely change this relationship.

### 1 Introduction

The ocean is an important sink for anthropogenic carbon ( $C_{\text{ant}}$ ) emissions from e. g. fossil fuel burning, cement production and land use change (Friedlingstein *et al.*, 2020). Over the industrial era, about 30 % of these emissions have been taken up by the ocean (Gruber *et al.*, 2019) (inferred from observations). Based on global biogeochemical models that meet observational constraints, Friedlingstein *et al.* (2020) find a slightly smaller ocean uptake of about 25 % of the emissions over the last decades. The decadal variability is smaller than  $\pm 5\%$ , indicating a minor contribution from changes in natural carbon. A small decrease in the fraction of the  $\text{CO}_2$  emissions taken up by the ocean is to be expected due to the decreasing buffer capacity of the oceanic waters. In addition, a slower oceanic circulation and mixing in a warming climate might reduce the uptake rate of surface waters for human-produced carbon (Heinze *et al.*, 2015). Future changes in the oceanic circulation may also alter the biological carbon pump and the storage of biogenic carbon (Heinze *et al.*, 2015).

The North Atlantic is the region with the highest column inventory of anthropogenic carbon (or the highest storage rates), both in models and observations (Sabine *et al.*, 2004; Khatiwala *et al.*, 2013). It is also a region with large variability in water mass formation, especially for Labrador Sea Water (Kieke *et al.*, 2006; Rhein *et al.*, 2007; Yashayaev, 2007; Kieke and



Yashayaev, 2015; Yashayaev and Loder, 2016). These changes in water mass formation/ventilation also have an impact on the inventories of  $C_{\text{ant}}$  (Steinfeldt et al., 2009; Pérez et al., 2013; Rhein et al., 2017). Our study addresses these impacts. It comprises the time frame with deep and intense formation of Labrador Sea Water (1987–1995) as well as the following period of weaker convection (1996–2013) (Kieke et al., 2007; Yashayaev, 2007; Kieke and Yashayaev, 2015). The recent reinvo-  
30 of deep reaching convection since 2014, accompanied with an increase in  $C_{\text{ant}}$  uptake and oxygen concentrations (Rhein et al., 2017) will not be considered here.

$C_{\text{ant}}$  in the ocean cannot be measured directly, but has to be inferred by indirect techniques. One group of methods to calculate  $C_{\text{ant}}$  concentrations are the so called “back calculation techniques”, (e. g.  $\Delta C^*$  (Gruber et al., 1996),  $\varphi C_T^0$  (Vázquez-Rodríguez et al., 2009)). These rely on measurements of dissolved inorganic carbon (DIC), the assumed natural background  
35 concentration of DIC, and the DIC originating both from the remineralization of organic matter and the dissolution of calcium carbonate. Another technique is the extended multiple linear regression (eMLR) (Friis et al., 2005). Here, observations at two times of both DIC and auxiliary quantities such as temperature, salinity, nutrients and oxygen are needed, which allow to build a regression for DIC based on the other variables. By this method, only the difference in  $C_{\text{ant}}$  between the two dates can be determined, but not the absolute value. Recently, Clement and Gruber (2018) developed an eMLR for  $C^*$ , i. e. the observed  
40 DIC excluding the carbon from remineralization of organic matter and dissolution of calcium carbonate. This eMLR( $C^*$ ) method has also been applied by Gruber et al. (2019) to the observational data from the GLODAPv2 data set.

Other methods do not rely on directly measured carbon data. Instead, they take advantage of anthropogenic tracers like CFCs and SF<sub>6</sub> and lead to  $C_{\text{ant}}$  distributions more compatible to these tracers. These methods are the transit time distribution (TTD) method (Hall et al., 2002; Waugh et al., 2006) and the Green’s function (GF) approach (Holzer and Hall, 2000; Khatiwala et  
45 al., 2013). They consider  $C_{\text{ant}}$  as a passive tracer that is advected from the surface into the ocean interior. Thus, these methods do not require to make assumptions about the biochemical involvement of carbon (the biological pump) as necessary for the aforementioned methods. Another advantage of the TTD technique – which will be exploited here – is to make predictions of  $C_{\text{ant}}$  concentrations from older observations - under the assumption that the ocean is in steady state. This allows to distinguish whether  $C_{\text{ant}}$  changes between two time period (i) originate from the atmospheric CO<sub>2</sub> increase or (ii) are caused by changes  
50 in the ocean circulation.

The different  $C_{\text{ant}}$  calculation methods lead in general to inventory differences of the order of  $\pm 10\%$ , both on the global scale (Khatiwala et al., 2013) as well as along basin-wide sections in the Atlantic (Vázquez-Rodríguez et al., 2009). However, the vertical distribution of the inventory is different, with the  $\Delta C^*$  method attributing a smaller fraction to the deep ocean (Vázquez-Rodríguez et al., 2009). This holds also for recently ventilated deep and bottom waters. On the regional scale, the  
55 inventory differences are larger, especially in the Southern Ocean (Vázquez-Rodríguez et al., 2009). For the biogeochemical consequences of oceanic  $C_{\text{ant}}$  storage like ocean acidification, not only the total oceanic  $C_{\text{ant}}$  uptake, but also its local storage rates as well as the vertical distribution are of importance.

Here, we use a modified version of the TTD method to infer the inventories of  $C_{\text{ant}}$  over the Atlantic from 70°S to 65°N for the years 1990, 2000, and 2010. The method is mainly based on Steinfeldt et al. (2009), but additionally allows for the  
60 admixture of old waters free of anthropogenic tracers. The impact of this modification of the TTD method on the derived  $C_{\text{ant}}$



**Table 1.** List of used cruises with transient tracer data not included in GLODAPv2.2019.

Cruise	Year	Data Availability
PE278	2007	<a href="https://doi.pangaea.de/10.1594/PANGAEA.911248">https://doi.pangaea.de/10.1594/PANGAEA.911248</a>
SUBPOARL08	2008	<a href="https://doi.pangaea.de/10.1594/PANGAEA.911310">https://doi.pangaea.de/10.1594/PANGAEA.911310</a>
PE319 <sup>a</sup>	2010	<a href="https://www.bodc.ac.uk/geotraces/data/idp2017/">https://www.bodc.ac.uk/geotraces/data/idp2017/</a>
PE321 <sup>a</sup>	2010	<a href="https://www.bodc.ac.uk/geotraces/data/idp2017/">https://www.bodc.ac.uk/geotraces/data/idp2017/</a>
M82/2	2010	<a href="https://doi.pangaea.de/10.1594/PANGAEA.911301">https://doi.pangaea.de/10.1594/PANGAEA.911301</a>
JC057 <sup>a</sup>	2011	<a href="https://www.bodc.ac.uk/geotraces/data/idp2017/">https://www.bodc.ac.uk/geotraces/data/idp2017/</a>
MSM21/2	2012	<a href="https://doi.pangaea.de/10.1594/PANGAEA.910957">https://doi.pangaea.de/10.1594/PANGAEA.910957</a>
MSM27	2013	<a href="https://doi.pangaea.de/10.1594/PANGAEA.911225">https://doi.pangaea.de/10.1594/PANGAEA.911225</a>
MSM28	2013	<a href="https://doi.pangaea.de/10.1594/PANGAEA.911234">https://doi.pangaea.de/10.1594/PANGAEA.911234</a>
MSM38	2014	<a href="https://doi.pangaea.de/10.1594/PANGAEA.911240">https://doi.pangaea.de/10.1594/PANGAEA.911240</a>
MSM39	2014	<a href="https://doi.pangaea.de/10.1594/PANGAEA.911243">https://doi.pangaea.de/10.1594/PANGAEA.911243</a>

<sup>a</sup>Part of GEOTRACES section GA02

concentrations will be described. We will then quantify the decadal  $C_{\text{ant}}$  inventories and their changes and compare them with a steady state ocean, where  $C_{\text{ant}}$  is solely changing due to the rising atmospheric  $\text{CO}_2$  concentration. This allows to determine the impact of changes in ocean ventilation and circulation on  $C_{\text{ant}}$ , i. e. the main processes storing  $C_{\text{ant}}$  in the ocean interior. We further discuss our results with respect to so far existing global studies and highlight and discuss prominent similarities and  
65 discrepancies.

## 2 Data and Methods

### 2.1 Data and calculation of decadal $C_{\text{ant}}$ distributions

We use anthropogenic tracers (CFC-12, CFC-11, CFC-113, tritium and  $\text{SF}_6$ ) to calculate transit time distributions (TTDs), from which finally the concentration of  $C_{\text{ant}}$  is inferred. The data is mainly taken from the GLODAPv2.2019 data product  
70 released in 2019 (Olsen *et al.*, 2019). The transient tracer data discussed here cover the time between 1982 and 2014. Also the GEOTRACES GAO2 section from 2010/2011 (Schlitzer *et al.*, 2018) and data from North Atlantic cruises conducted over the period 2007–2014 and not contained in this data product have been added here (Table 1).

The data are grouped into three decades roughly centered around 1990, 2000, and 2010. Data from the years 1982–1994, 1995–2005, and 2006–2014 are used for the three periods. Data from 2014 in the central Labrador Sea, which is characterized  
75 by the local reinvocation of deep convection (Yashayaev and Loder, 2016) has been excluded. Table 2 shows the number of available tracer data for each of these periods. The location of all profiles with CFC-12 and/or CFC-11 data for the three decades are indicated in Fig. 1. Tritium, CFC-113 and  $\text{SF}_6$  are collocated with CFC-11/CFC-12, but have much lesser data



**Table 2.** Number of anthropogenic tracer samples used for the  $C_{\text{ant}}$  calculation.

Time period	Number of samples			
	CFC-12 or CFC-11	SF <sub>6</sub>	CFC-113 <sup>a</sup>	Tritium <sup>a</sup>
1982–1994	48,595	0	5,242	1,265
1995–2005	80,063	1,864	26,912	991
2006–2014	34,836	11,571	8,650	13

<sup>a</sup>CFC-113 and tritium are only used to calculate the ratio of width over mean age of the TTDs, independent from time.

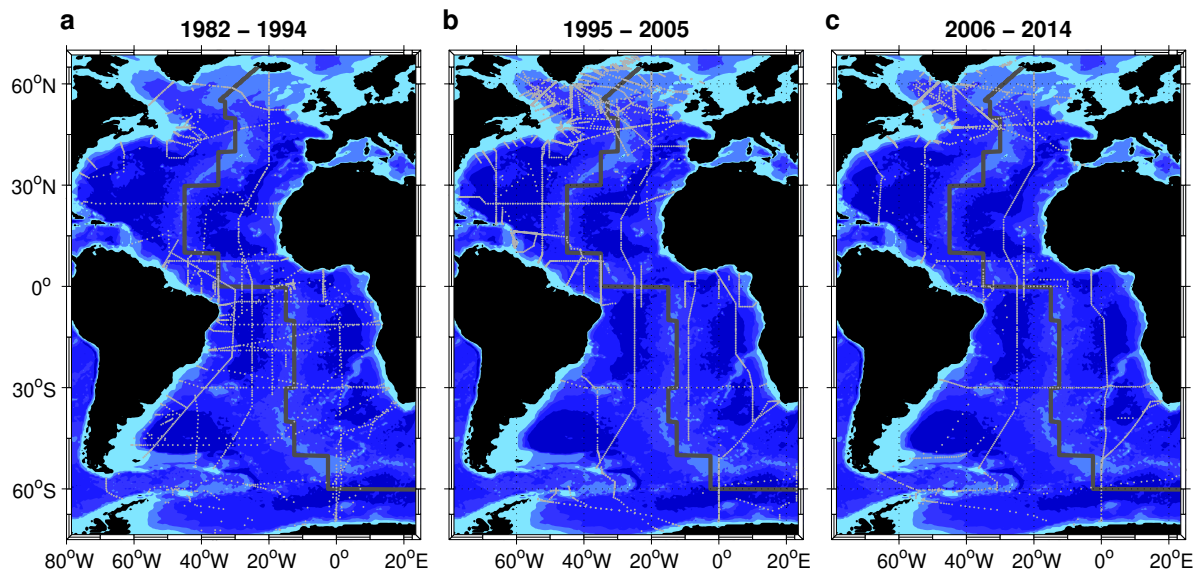


**Figure 1.** Location of ship stations with CFC-12 or CFC-11 data used for the  $C_{\text{ant}}$  calculation for the three decades considered here. a: 1982–1994, b: 1995–2005, c: 2006–2014. The thick grey line following the Mid-Atlantic Ridge is used for separating the Atlantic Ocean into a western and eastern basin.

points. For each data profile, means for 38 isopycnal layers of salinity, potential temperature, the inferred  $C_{\text{ant}}$  and in addition the thickness of each layer have been calculated. The boundaries of the isopycnal layers are given in Table A1 (Appendix).

80 There, also additional information on the isopycnal interpolation can be found. The isopycnal means of the anthropogenic tracers are used to compute  $C_{\text{ant}}$ , as described in section 2.3.

The aforementioned isopycnal mean values are then mapped horizontally (i. e. isopycnally) on a regular grid (0.5° longitude  $\times$  0.25° latitude) from 70°S to 65°N and 80°W to 20°E. The gridding procedure is similar to that applied in Rhein et al. (2015), i. e. an objective mapping scheme is used, where the weighting factor decreases with distance  $r$  from the data  
85 points ( $\exp(-r^2)$ ). An additional weighting factor proportional to  $\exp(-\Delta(f/H)^2)$  ( $f$ : Coriolis parameter,  $H$ : water depth,



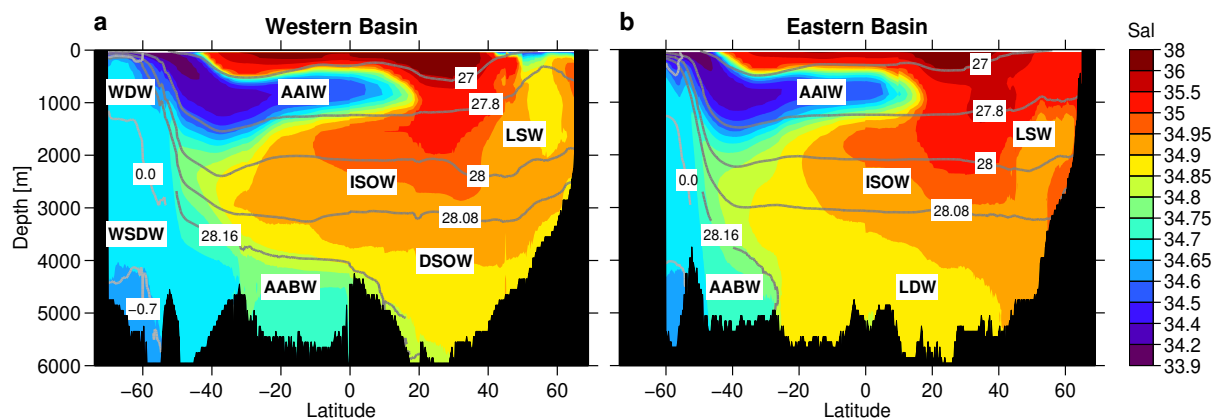


**Figure 2.** Zonal mean sections of salinity, a: western Atlantic basin, b: eastern Atlantic basin. Contour lines show zonally averaged neutral density isopycnals  $\gamma_n$  (dark grey) and isotherms (light grey,  $\theta = 0.0^\circ\text{C}$  and  $\theta = -0.7^\circ\text{C}$ , south of  $50^\circ\text{S}$  only) as boundaries of the main water masses. For acronyms of water masses see text.

$\Delta(f/H)$ : difference in  $f/H$  between grid point and data point), which results in a terrain following interpolation, is only applied to the  $\sigma_{1.5}$  and  $\sigma_4$  density levels, as the upper lighter waters are less constrained by topography. The marginal seas like Mediterranean, Caribbean and North Sea are excluded from the gridded data. Density is vertically interpolated every 100m and horizontally mapped in the same way as the other quantities. The gridding is done separately for the data from the three decades. Additionally, all data from the whole period 1982–2014 are pooled together to produce climatologies for density, salinity, and  $C_{\text{ant}}$ . The gridded fields for the individual decades in some locations have gaps due to sparse input data. This is not the case for the gridded climatological fields based on the entire data set. In these cases, the gaps of the respective decadal fields are filled by the values obtained from the climatology. For the periods 1982–1994 and 1995–2005, about 10% of the decadal gridded values are missing, for the period 2006–2014, where the data gaps are larger (Fig. 1), it is 20%.

95 From the gridded data we compute column inventories for  $C_{\text{ant}}$  as well as mean vertical sections. For the column inventories, the  $C_{\text{ant}}$  concentrations for each isopycnal layer are multiplied with the density and layer thickness, and then integrated vertically. This results in an inventory of  $C_{\text{ant}}$  per square meter. In addition,  $C_{\text{ant}}$  and salinity are studied along two meridional sections that represent zonal means over the western and eastern basin of the Atlantic. The separation line mainly follows the course of the Mid-Atlantic Ridge (see Fig. 1). Selected isopycnals of neutral density  $\gamma_n$  from the 'climatological' density fields are also shown in the section plots to give a rough overview on the distribution/location of the main water masses as described below.

## 2.2 Major water masses and their definition

The distribution of  $C_{\text{ant}}$  is inevitably linked to the spreading of the different water masses. We thus give a short overview over the major water masses in the Atlantic. The zonal mean salinity sections for the western and eastern Atlantic indicate the position of the main water masses (Fig. 2). The areas with high salinities reaching down to 400 – 600m depth between



20°S – 40°S and 20°N – 40°N belong to the Subtropical Mode Waters (STMW). These are formed in the subtropical gyres by buoyancy loss and subduction (Talley, 1999). Further north in the eastern basin, the upper few hundred meters are covered by Subpolar Mode Water (SPMW) (Brambilla and Talley, 2008), which also has a relatively high salinity ( $> 35$ ). The deeper region with salinities  $> 35.5$  around 1000m and 40°N in the eastern basin is dominated by the Mediterranean Outflow Water (MOW). As can be seen from the salinity distribution, this water mass penetrates further into the western basin and also mixes into the underlying North Atlantic Deep Water (NADW).

The low salinity tongue at around 1000m stretching from 45°S – 20°N marks the Antarctic Intermediate Water (AAIW). This water mass is formed at the Subantarctic Front at about 45°S by ventilation of Subantarctic Mode Water (SAMW) formed in the southeast Pacific and Drake Passage (McCartney, 1982). It even reaches the subpolar North Atlantic, but loses its characteristic salinity minimum (Álvarez *et al.*, 2004).

The most prominent deep water mass is the North Atlantic Deep Water, which consists of different components, i. e. Labrador Sea Water (LSW), Iceland-Scotland Overflow Water (ISOW) and Denmark Strait Overflow Water (DSOW). The LSW is formed in the northwestern subpolar Atlantic by deep convection, occasionally reaching down to 2000m (Lazier *et al.*, 2002; Yashayaev, 2007; Kieke and Yashayaev, 2015). The salinity minimum associated with this newly formed LSW is clearly seen in Fig. 2a between 50°N and 60°N. When spreading south- and eastward, the salinity of LSW increases due to mixing with surrounding more saline water masses, especially MOW. The ISOW enters the subpolar North Atlantic via the Iceland-Scotland Ridge. It entrains ambient waters such as SPMW (Mauritzen *et al.*, 2005), which leads to the relatively high salinity of this water mass (see the salinity maximum in Fig. 2b at 60°N between 2000m and 3000m depth). Further downstream, the ISOW also entrains fresher LSW (Dickson *et al.*, 2002), leading to a salinity decrease. Large parts of the ISOW enter the western basin mainly via the Charlie-Gibbs and the Bight Fracture Zones (McCartney, 1992; Petit *et al.*, 2018), while a smaller part continues southward in the eastern basin (Fleischmann *et al.*, 2001).

The densest component of NADW is the DSOW. South of Denmark Strait between Greenland and Iceland, this water spreads close to the bottom and entrains ambient waters (Jochumsen *et al.*, 2015). It is less saline than the ISOW above. Due to its high density and great depth (below  $\approx 3500$ m), it cannot enter the eastern Atlantic directly.

In the Southern Ocean, NADW succumbs to upwelling and gets incorporated into the Circumpolar Deep Water (CDW) (Judicone *et al.*, 2008). The southernmost extension of CDW between the Antarctic Continent and the Antarctic Circumpolar Current is called Warm Deep Water (WDW). This water also contains older deep water from the other oceans and more recently ventilated water from the Weddell Sea in the Atlantic Sector of the Southern Ocean (Klatt *et al.*, 2002).

The water mass close to the bottom with relatively low salinity is the Antarctic Bottom Water (AABW). In the Atlantic, AABW is formed in the Weddell Sea including subsurface excursions of saline shelf water below the ice shelf and substantial entrainment of WDW when descending into the abyss. It leaves the Southern Ocean guided by topography into the deep basins of the western Atlantic (Bullister *et al.*, 2013). Major pathways for deep and bottom waters to flow into the eastern basins are the Romanche Fracture Zone (Mercier and Morin, 1997) near the equator and the Vema Fracture Zone at 11°N (Fischer *et al.*, 1996). This eastward penetration of AABW at the equator is visible by a salinity minimum directly above the bottom. The intensified vertical mixing with the overlying DSOW as observed in the Romanche Fracture Zone (Mercier and Morin, 1997)



145 makes the bottom waters of the eastern basin more saline than in the western part. At the same time, the temperature increases and the density decreases. This altered AABW in the eastern basin is then called Lower Deep Water (LDW). The further salinity increase in the deep eastern Atlantic towards the northern boundary might be explained by intrusion of the densest part of ISOW. Nevertheless, the influence of AABW is still visible, e. g. by enhanced noble gas concentrations observed along  
145 60°N originating from the entrainment of subglacial melt water from the Antarctic ice shelves (*Rhein et al.*, 2018).

South of the fronts of the Antarctic Circumpolar Current, at about 55°S, the densities of the deep water are considerably higher. There, the potential temperature  $\theta$  is used to distinguish between Warm Deep Water (WDW,  $\theta > 0^\circ\text{C}$ ) Weddell Sea Deep Water (WSDW,  $0^\circ\text{C} > \theta > -0.7^\circ\text{C}$ ), and the Weddell Sea Bottom Water (WSBW,  $\theta < -0.7^\circ\text{C}$  (*van Heuven et al.*, 2011)). WSBW, WSDW and WDW are precursor water masses of AABW.

150 The neutral density boundaries of some specific water masses are shown in all the section figures. We selected the boundaries according to the salinity distribution, i. e. the low salinity tongue of the AAIW is comprised by the isopycnals  $\gamma_n = 27.0\text{ kg m}^{-3}$  and  $\gamma_n = 27.8\text{ kg m}^{-3}$ . For the NADW components, we roughly follow the values given in *Le Bras et al.* (2017). Only for the density at the lower boundaries of LSW and ISOW we use slightly denser isopycnals to better represent the salinity distribution. With the water mass boundaries shown in Fig. 2 the salinity minimum of the LSW in the northwest Atlantic and the salinity  
155 maximum of the ISOW at the northern boundary of the eastern basin are contained completely in the respective water mass. For the boundary between DSOW and AABW we have chosen the isopycnal  $\gamma_n = 28.16\text{ kg m}^{-3}$ , almost following the isohaline  $S = 34.85$ . This leads to a northern boundary of AABW in the western basin at around 20°N. There are some extensions of AABW found further north, but they have mixed with the overlying DSOW and are thus more saline and also more enriched in anthropogenic tracers.

## 160 2.3 Anthropogenic carbon inferred from the TTD method

In this paper, we use a modified TTD method to infer the concentration of  $C_{\text{ant}}$ . This is based on the method used in *Steinfeldt et al.* (2009). In addition, we explicitly allow for the admixture of old, tracer free waters. This approach has been used before, e. g. in *Steinfeldt and Rhein* (2004), but there it was locally restricted to the deep western boundary current in the tropics and was not used to calculate anthropogenic carbon. Here, we introduce a new algorithm that allows to assign the admixture of old  
165 water at any location.

### 2.3.1 The standard TTD method

First, we explain the standard TTD method by following the procedure in *Hall et al.* (2002). Due to the advective-diffusive nature of the oceanic transport, the water in the ocean interior consists of fluid elements with different pathways and ages (time elapsed since the water parcel left the mixed layer). The distribution of these ages is described by the TTD function  $\mathcal{G}$ . The  
170 concentration of any conservative property  $C(x, t)$  at location  $x$  in the ocean interior and time  $t$ , which can be a particular



reference year  $t_{\text{ref}}$ , is then given by

$$C(\mathbf{x}, t_{\text{ref}}) = \int_0^{\infty} C^0(t_{\text{ref}} - \tau) \mathcal{G}(\mathbf{x}, t_{\text{ref}}, \tau) d\tau \quad (1)$$

(Hall *et al.*, 2002), where  $\tau$  denotes the age of the water.  $C^0(t)$  is the concentration history of the property in surface waters in the mixed layer. For upper water masses, we assume that  $C^0(t)$  for CFCs and  $\text{SF}_6$  is in solubility equilibrium with the atmosphere. For deeper, denser waters, the saturation decreases gradually to 80%. A detailed list of the saturation used for each density layer is given in the Supporting Information, Table A1. In Steinfeldt *et al.* (2009), the minimum saturation was chosen lower, i. e. 65%. However, CFC concentrations measured close to the formation region of NADW tend to be larger than 65% of the surface saturation (see Fig. B1), so the value for the minimum CFC saturation has been enlarged for all dense water data. According to Steinfeldt *et al.* (2009), the difference in the resulting  $C_{\text{ant}}$  concentrations is about half the saturation difference, i. e. about 10%. For  $C_{\text{ant}}$ , we use a time independent carbon disequilibrium and a saturation of 100%, as in Waugh *et al.* (2006) and Steinfeldt *et al.* (2009).  $C_{\text{ant}}(t_{\text{ref}})$ , is calculated as the difference between the carbon concentration at time  $t_{\text{ref}}$  and the preindustrial time (year 1780). If the carbon disequilibrium remains constant, it cancels out when calculating this difference.

Eq.(1) will be used to infer concentrations of anthropogenic carbon ( $C_{\text{ant}}(\mathbf{x}, t)$ ) from the TTD functions  $\mathcal{G}(\mathbf{x}, t, \tau)$ . On the other hand, Eq.(1) allows to infer the parameters of the TTD, such that  $C(\mathbf{x}, t)$  are observed tracer concentrations. To do so, a certain functional form of the TTD has to be assumed. Here, we apply an inverse Gaussian function as approximation for the TTD, as has been done in other studies (e. g. Hall *et al.* (2002); Waugh *et al.* (2006); Steinfeldt *et al.* (2009)). This function only depends on two parameters: the mean age  $\Gamma$  (first moment associated with the advective tracer transfer) and the width  $\Delta$  (second moment, which is related to the dispersion or mixing on all relevant scales, including recirculation and admixtures or entrainment of older water):

$$\mathcal{G}(\tau, \Gamma, \Delta) = \sqrt{\frac{\Gamma^3}{4\pi\Delta^2\tau^3}} \exp\left(\frac{-\Gamma(\tau - \Gamma)^2}{4\Delta^2\tau}\right). \quad (2)$$

In order to derive both parameters ( $\Delta$  and  $\Gamma$ ), simultaneous measurements of different anthropogenic tracers would be needed. As these are sparse, a fixed ratio of  $\Delta/\Gamma$  is often used. This ratio is a measure for the importance of mixing (higher  $\Delta/\Gamma$  values imply stronger mixing). Waugh *et al.* (2004) inferred a ratio of  $\Delta/\Gamma = 1$  from tracer observations in the subpolar North Atlantic.

In an ideal case, if  $\mathcal{G}$  would be the “real” TTD, the mean age  $\Gamma$  should be independent of the tracer from which it is inferred. Eq.(1) then holds for CFC-12, CFC-11,  $\text{SF}_6$  and any other tracer taken from the same water sample with identical TTD parameters. In reality, if Eq. 1 holds for one tracer (e. g CFC-12) with the regional  $\Delta/\Gamma$  value, applying Eq. 1 with the same parameters of  $\mathcal{G}$  to another tracer (e. g. CFC-11) may result in deviations of the order of a few % to the observed CFC-11 concentration. In this study, we use preferably CFC-12 derived ages, only when CFC-12 is not available, we use CFC-11. The number of the available/considered age data points is given in Table 1. CFC-12 and CFC-11 are the most commonly measured tracers (Table 2). The advantage of CFC-12 is that it has increased in the atmosphere prior to CFC-11 and, for the recent years,



**Table 3.** Hemispheric and total Atlantic  $C_{\text{ant}}$  inventories referenced to 2010 for three different methods: the standard TTD method (as used e. g. in *Waugh et al.* (2006)), a variable  $\Delta/\Gamma$  ratio (as used in *Steinfeldt et al.* (2009)), and the modified TTD method with both a variable  $\Delta/\Gamma$  ratio and an explicit dilution factor  $f$ .

	Standard Cant [Pg C]	Var. $\Delta/\Gamma$ Cant [Pg C]	Var. $\Delta/\Gamma$ and dil. $f$ Cant [Pg C]
North	32.4	31.7	30.2
South	30.5	29.6	25.2
Total	63.0	61.3	55.4

shows a smaller decline. For young waters, this decline leads to relatively large errors (from measurement uncertainties and an unknown mixed layer saturation) of the age and for the inferred anthropogenic carbon (*Tanhua et al.*, 2008). Thus, for data after 2005 in the upper layers with young water (central and intermediate waters) and relatively high  $\text{SF}_6$  concentrations, we use the  $\text{SF}_6$  based age estimate, if available. In the subpolar Atlantic north of  $45^\circ\text{N}$ , the density range for using the  $\text{SF}_6$  age is expanded into the Labrador Sea Water, as this water mass there has also relatively young ages.

*Steinfeldt et al.* (2009) used pointwise TTDs with  $\Delta/\Gamma$  ratios of 0.5, 1, or 2 for the subpolar to tropical Atlantic based on simultaneous observations of CFC-12/tritium and CFC-12/CFC-113. Here, we also make use of simultaneous measurements of CFC-12 and  $\text{SF}_6$  to infer the  $\Delta/\Gamma$  ratio and also rounded it to the quantized values of 0.5, 1, or 2. Note that  $\text{SF}_6$  is not used in the deep and bottom waters, as the concentrations could still be enlarged from the remnants of artificial tracer release experiments in the 1990s in the Nordic Seas (*Watson et al.*, 1999; *Tanhua et al.*, 2005) and Brazil Basin (*Polzin et al.*, 1997). Tritium is only used north of  $45^\circ\text{N}$ . This excludes southern sources with lower surface tritium values. Including those would imply a spatial dependence of  $C^0$  in Eq.(1), which is not applied here.

As in *Steinfeldt et al.* (2009), the inferred  $\Delta/\Gamma$  ratios are gridded for each isopycnal layer in the same way as the other data (see section 2.1). Due to the limited amount of tritium, CFC-113 and  $\text{SF}_6$  observations compared to CFC-12, the data from all three decades are combined and any temporal change of the  $\Delta/\Gamma$  ratio is not accounted for. Remaining data gaps of the gridded fields are filled with the standard value of  $\Delta/\Gamma = 1$ . The distribution of the resulting  $\Delta/\Gamma$  ratios is shown in Fig. 3 a and b for the western and eastern basin of the Atlantic. We find high ratios close to the maximum value of 2 at the surface and in the newly formed AAIW, NADW (LSW, ISOW, DSOW) and AABW. For the latter, directly North of Antarctica  $\Delta/\Gamma$  is about unity, and the higher  $\Delta/\Gamma$  ratios are found only in the region of the Antarctic Circumpolar Current. Only the subtropical mode waters have  $\Delta/\Gamma$  ratios below 1 near their formation region. Further downstream, the  $\Delta/\Gamma$  ratio of the intermediate, deep and bottom waters decreases towards unity and even below, especially for LSW in the northeastern Atlantic.

The difference between the  $C_{\text{ant}}$  concentrations based on the variable  $\Delta/\Gamma$  ratio and the case that  $\Delta/\Gamma = 1$  is depicted in Fig. 3 c and d (here, the climatological  $C_{\text{ant}}$  fields referenced to 2010 are used). In general,  $\Delta/\Gamma > 1$  leads to smaller, and  $\Delta/\Gamma < 1$  to larger values of the inferred  $C_{\text{ant}}$ . The areas with the  $\Delta/\Gamma > 1$  dominate, but the basinwide reduction of the  $C_{\text{ant}}$  inventory due to the variable  $\Delta/\Gamma$  ratio is only of the order of 1 Pg C (see Table 3) both for the North and the South Atlantic.

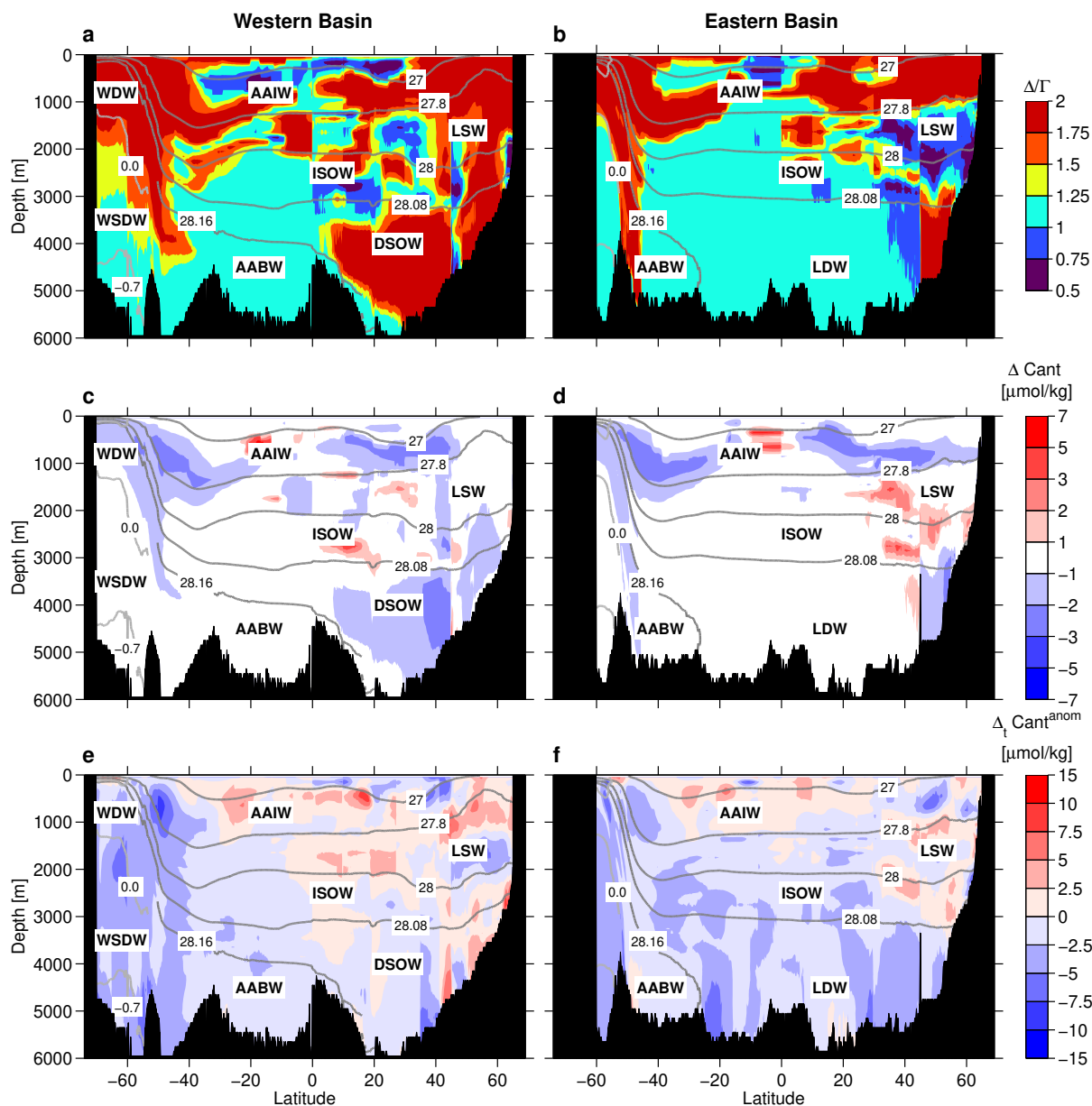


**Figure 3.** a–b: Zonal mean sections showing the  $\Delta/\Gamma$  ratio inferred from simultaneous observations of different tracers. c–d: Difference in zonal mean  $C_{\text{ant}}$  concentrations calculated from a variable  $\Delta/\Gamma$  ratio and from the constant ratio of  $\Delta/\Gamma = 1$ . The  $C_{\text{ant}}$  fields are based on tracer data from the whole period (1982–2014), the reference year is 2010. e–f: Zonal mean sections of  $\Delta_t C_{\text{ant}}^{\text{anom}}$  for a variable  $\Delta/\Gamma$  ratio ( $C_{\text{ant}}$  calculated for 2010 with data around 2010 minus  $C_{\text{ant}}$  calculated for 2010 based on tracer data around 1990, i. e.  $C_{\text{ant}}^{2010} - C_{\text{ant}}^{1990 \rightarrow 2010}$ ). Contour lines are shown as in Fig. 2. For details see text.





One advantage of the TTD method is that it allows for the choice of the reference year  $t_{\text{ref}}$  in Eq.(1). This makes it possible to group observations from several years to calculate  $C_{\text{ant}}$  for a common reference year, as it has been done here for CFC/SF<sub>6</sub> data from 1982–1994, 1995–2005, 2006–2014 and using all data from 1982–2014. By varying  $t_{\text{ref}}$  in Eq. (1), the TTD method also allows to make predictions for future tracer concentrations. If the TTD parameters have been determined from a tracer observation at time  $t_{\text{obs}}$ ,  $t_{\text{ref}}$  can be shifted into the future and the concentration of any tracer can be inferred from Eq.(1) for this future time  $t_{\text{ref}}$ . The assumption underlying this prediction is that the TTD function  $\mathcal{G}$  remains the same,  $\mathcal{G}(\mathbf{x}, t_{\text{obs}}, \tau) = \mathcal{G}(\mathbf{x}, t_{\text{ref}}, \tau)$ , i. e. the ocean circulation and ventilation does not change. The increase of  $C_{\text{ant}}$  in this case is thus only due to the rising atmospheric CO<sub>2</sub>.

In particular, we use the tracer data from around 1990 (1982–1994) to predict  $C_{\text{ant}}$  for the reference year 2010. These predicted  $C_{\text{ant}}$  values are denoted by  $C_{\text{ant}}^{1990 \rightarrow 2010}$ . This prediction can be compared with the case where  $C_{\text{ant}}$  is inferred from data around the reference year.  $C_{\text{ant}}^{2010}$ , e. g. means  $C_{\text{ant}}$  calculated from data between 2006–2014 and referenced to the year 2010. The difference  $C_{\text{ant}}^{2010} - C_{\text{ant}}^{1990 \rightarrow 2010}$  can be interpreted as anomaly of the  $C_{\text{ant}}$  increase (or accumulation) between 1990 and 2010 due to changes in the oceanic circulation/ventilation (i. e. in the TTDs) and will thus be denoted  $\Delta_t C_{\text{ant}}^{\text{anom}}$ , as in Gruber *et al.* (2019). These anomalies can also be inferred for the other decadal  $C_{\text{ant}}$  increase rates, i. e.  $C_{\text{ant}}^{2000} - C_{\text{ant}}^{1990 \rightarrow 2000}$  and  $C_{\text{ant}}^{2010} - C_{\text{ant}}^{2000 \rightarrow 2010}$ .

Fig. 3 e–f show the distribution of  $\Delta_t C_{\text{ant}}^{\text{anom}}$  for the western and eastern basin for the case  $C_{\text{ant}}^{2010} - C_{\text{ant}}^{1990 \rightarrow 2010}$ . The features of this distribution will be discussed in detail in section 3.3.2. Here, we only want to point out that in some cases large anomalies are found in the formation region of a water mass, e. g. for LSW and AAIW in the western Atlantic. Further downstream, around 20°N for LSW and 20°S for AAIW, the anomalies are slightly smaller. This is to be expected, as away from the source region waters from different vintages with different  $C_{\text{ant}}$  anomalies mix. However, we also find strongly negative values of  $\Delta_t C_{\text{ant}}^{\text{anom}}$  in the LDW in the eastern Atlantic, which is the oldest water mass and not in the direct export path way of AABW or DSOW. In these old waters, a pronounced  $C_{\text{ant}}$  anomaly should only occur for a pronounced longtime change in the ocean circulation/ventilation. But even then, the  $C_{\text{ant}}$  accumulation anomaly should be smaller than in the regions with high  $C_{\text{ant}}$  concentrations like the water mass formation regions. Older waters contain a notable fraction with ages larger than 200 yr (see the example in Table C1), i. e.  $C_{\text{ant}}$  free waters, which cannot contribute to the  $C_{\text{ant}}$  anomaly. We thus consider the strongly negative  $\Delta_t C_{\text{ant}}^{\text{anom}}$  values in LDW as an artefact of the TTD parameterization in the form of a single inverse Gaussian function. In the next section we show how a modification of the TTD parameterization by including an additional dilution of young with old waters helps to overcome this artefact.

### 2.3.2 The modified TTD method with dilution

Steinfeldt and Rhein (2004) presented the foundation of the TTD method applied here by focusing on the Deep Western Boundary Current (DWBC) of the tropical Atlantic and investigating the NADW therein as a mixture of young and old water contributions. We will apply the same principle here, but in contrast to the previous study extend this approach to the entire

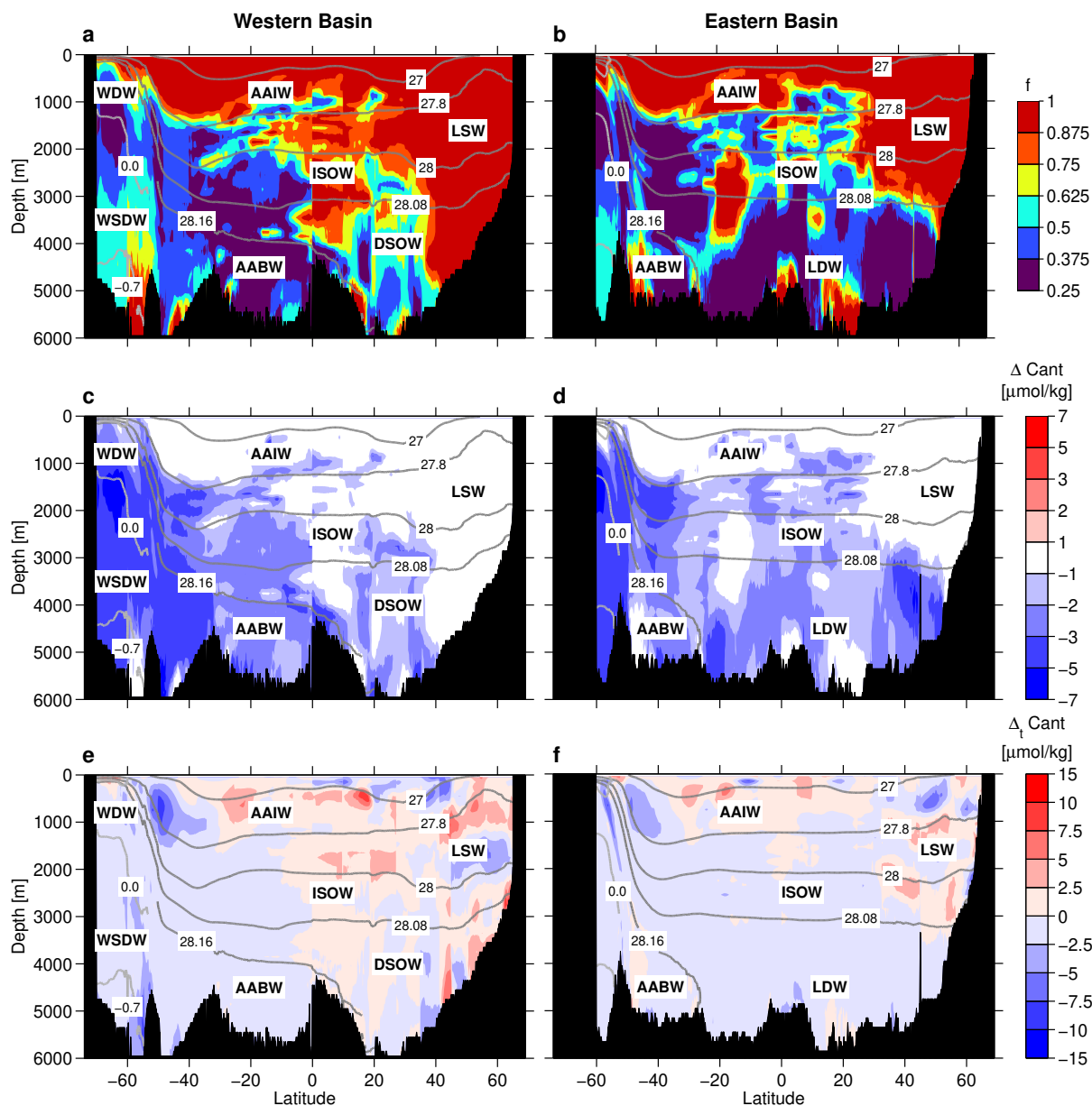


**Figure 4.** a–d: Zonal mean sections showing the fraction  $f$  of young,  $C_{ant}$  bearing water. c–d: Difference in zonal mean  $C_{ant}$  concentrations between the cases with variable fraction  $f$  and no dilution ( $f = 1$ ). The  $C_{ant}$  fields are based on tracer data from the whole period (1982–2014), and the reference year is 2010. e–f: Zonal mean sections of  $\Delta_t C_{ant}^{anom}$  for a variable  $\Delta/\Gamma$  ratio ( $C_{ant}$  calculated for 2010 with data around 2010 minus  $C_{ant}$  calculated for 2010 based on tracer data around 1990, i. e.  $C_{ant}^{2010} - C_{ant}^{1990 \rightarrow 2010}$ ). Contour lines are shown as in Fig. 2. For details see text.



260 Atlantic Ocean.

$$\mathcal{G} = f \cdot \mathcal{G}_{\text{young}} + (1 - f) \cdot \mathcal{G}_{\text{old}} \quad (3)$$

$\mathcal{G}_{\text{old}}$  is assumed to not contain CFCs and also no  $C_{\text{ant}}$ , thus we do not need to consider it here. The additional parameter  $f$  describes the fraction of younger water, and  $1 - f$  the “dilution” with old water. Eq. 1 then becomes:

$$C(\mathbf{x}, t_{\text{ref}}) = \int_0^{\infty} C^0(t_{\text{ref}} - \tau) \cdot f \cdot \mathcal{G}_{\text{young}}(\mathbf{x}, t_{\text{ref}}, \tau) d\tau. \quad (4)$$

265 The dilution of younger water with an old component can be interpreted as follows: In the North Atlantic, the younger water can be regarded as NADW, and the old water as admixtures of AABW or recirculated NADW. In the South Atlantic, young waters are AABW and AAIW, and the old water originates from NADW. We also introduce an age threshold below which the dilution case is excluded. This is chosen as  $\Gamma_{\text{young}} = 100 \text{ yr}$ . Thus it is guaranteed that for relatively young waters, e. g. in the vicinity of water mass formation regions, only the no dilution case is applied.

270 In order to determine  $f$ , *Steinfeldt and Rhein* (2004) used assumptions that are only valid in the DWBC. Here, we want to apply the dilution at any region, especially for old water like the LDW, far away from the DWBC. The method to determine the fraction  $f$  is as follows: For  $f = 1$ , we calculate  $C_{\text{ant}}$  as described above with the  $\Delta/\Gamma$  ratios determined from simultaneous observations of different transient tracers. In addition, we infer  $C_{\text{ant}}$  for values of  $f$  of 0.75, 0.5, and 0.25 with  $\Delta/\Gamma = 1$ . These quantized values are chosen to limit the computational effort and obtain marked differences between the derived  $C_{\text{ant}}$  concentrations. From the four sets of TTD parameters four different  $C_{\text{ant}}$  values are inferred.

At each grid point, from these four TTD parameterizations that one is chosen which minimizes the  $C_{\text{ant}}$  anomalies  $\Delta_t C_{\text{ant}}^{\text{anom}}$  between all decadal values, i. e.:

$[\min(C_{\text{ant}}^{2000} - C_{\text{ant}}^{1990 \rightarrow 2000})^2 + (C_{\text{ant}}^{2010} - C_{\text{ant}}^{2000 \rightarrow 2010})^2 + (C_{\text{ant}}^{2010} - C_{\text{ant}}^{1990 \rightarrow 2010})^2]$ . In the case that the gridded  $C_{\text{ant}}$  fields have gaps for one or more of the three decadal fields,  $f$  is set to 1. An example for the influence of varying the TTD parameters

280 ( $\Delta/\Gamma$  ratio, fraction  $f$ ) is given in Fig. C1.

The inferred fractions  $f$  are shown in Fig. 4a–b for the western and eastern basin. Close to the water mass formation regions, e. g. the subpolar North Atlantic, the waters are too young to allow for a dilution, so  $f$  is set to 1 there. A strong dilution with old waters (low  $f$ ) is mainly found in the deep and bottom waters in the tropical and South Atlantic, in parts of the WDW and WSDW in the Southern Ocean and in the LDW in the North eastern Atlantic. In these regions, the inferred  $C_{\text{ant}}$  concentrations are remarkably smaller than for the case without dilution (see Fig. 4c–d). In general, the regions with  $f < 1$  always show a reduction in  $C_{\text{ant}}$ . For the North Atlantic, where the regions with  $f = 1$  dominate, the basinwide  $C_{\text{ant}}$  inventory is only reduced by about 1 Pg C compared to the TTDs without dilution. For the South Atlantic, this reduction is larger, more than 4 Pg C (Table 3).

290 The introduction of the dilution  $f$  does not only lead to smaller  $C_{\text{ant}}$  concentrations, but also to a reduction of the amount of the  $C_{\text{ant}}$  accumulation anomalies  $\Delta_t C_{\text{ant}}^{\text{anom}}$ . A comparison between Fig. 3 e–f and 4 e–f shows that  $\Delta_t C_{\text{ant}}^{\text{anom}}$  becomes less negative especially in the waters of Antarctic origin (WSDW, AABW and LDW), where  $f < 1$ . On the other hand, the

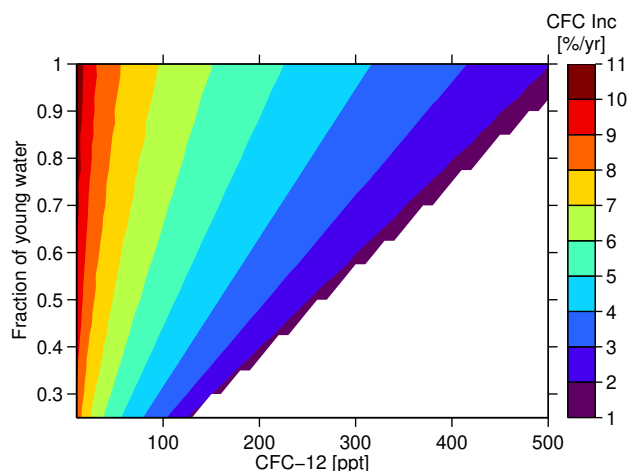


**Figure 5.** Expected increase rate (Inc) per year of CFC-12 for a concentration observed in year 2000 as a function of the observed CFC-12 concentration itself and the fraction of young water. High CFC-12 concentrations are incompatible with low fractions of young water, this area is left blank. For details see text.

positive  $C_{\text{ant}}$  anomalies in the NADW, especially the LSW, in the western tropical Atlantic hardly change, i. e. they are less dependent from the parameterization of the TTDs. In section 3.3.2 we will relate these  $C_{\text{ant}}$  accumulation anomalies with observed changes in ocean ventilation. As the spuriously negative values of  $\Delta_t C_{\text{ant}}^{\text{anom}}$  in the old deep waters are reduced by taking into account the dilution of young with old water, we will use the modified TTDs with dilution to compute the Atlantic  $C_{\text{ant}}$  inventories. Another advantage of this TTD parameterization is that it reduces the relatively high  $C_{\text{ant}}$  concentrations in the Southern Ocean that results from the standard TTD method compared to other  $C_{\text{ant}}$  calculation techniques (Waugh *et al.*, 2006; Vázquez-Rodríguez *et al.*, 2009; Khatiwala *et al.*, 2013).

The strongly negative  $C_{\text{ant}}$  accumulation anomalies, when using the standard TTDs, indicate that the water in 2010 is older than in 1990, thus  $C_{\text{ant}}$  calculated from the age in 1990 with reference year 2010 is larger than  $C_{\text{ant}}$  derived from the age in 2010. Fig. 5 shows, that the CFC-increase rate for a steady state ocean (calculated from Eq.(1)) for CFC-12 in the year 2000 is smaller for smaller fractions  $f$ . If an observed CFC increase over time lags the expected value from Fig. 5, the water becomes older, and vice versa. Thus, the choice of the dilution factor  $f$  influences inferred age changes of the water masses over time, and, as a consequence, the magnitude of the  $C_{\text{ant}}$  anomaly  $\Delta_t C_{\text{ant}}^{\text{anom}}$ .

### 2.3.3 Error estimation

The error of  $C_{\text{ant}}$  is calculated in a similar way as in Steinfeldt *et al.* (2009). The contributions of the interpolation/gridding error (3%), the  $C_{\text{ant}}$  disequilibrium (possible undersaturation) (20%), the CFC disequilibrium (5.5%, including errors in the CFC measurements) are treated in the same way. The value of the interpolation/gridding error is confirmed here when comparing the  $C_{\text{ant}}$  inventories calculated for the decadal data (1982–1994, 1995–2005, and 2006–2014 respectively) and all data (Table



310 4). The number of all data points is about three times as large as for the decadal data sets, but the inferred  $C_{\text{ant}}$  inventory is quite similar (the largest discrepancy is about 4% for the South Atlantic in 2010). The  $C_{\text{ant}}$  uncertainty in very old waters of  $2.0 \mu\text{mol kg}^{-1}$  (Steinfeldt *et al.*, 2009) is considered as minimum error everywhere. If the CFC-12 concentration is below the typical detection limit of  $0.005 \text{ pmol kg}^{-1}$ , the  $C_{\text{ant}}$  concentration is set to zero. The error due to the TTD parameterization as an Inverse Gaussian function compared to the “real” TTD is the maximum of the 20% given in Steinfeldt *et al.* (2009) and the  
315 difference in  $C_{\text{ant}}$  calculated with the standard TTD method and the case with dilution.

All these errors apply to the  $C_{\text{ant}}$  value at each data point. For the gridded fields, the statistical errors reduce according to the degrees of freedom, whereas the systematic errors remain unchanged. The errors due to the shape of the TTD and the unknown  $C_{\text{ant}}$  disequilibrium are assumed to be similar (or systematic) within one water mass, but may vary between water masses. As there are about four different water mass classes (Central and Intermediate Water, LSW, Overflow Waters, and AABW), these  
320 errors are divided by  $\sqrt{4} = 2$  when the error over the whole water column is considered. The  $C_{\text{ant}}$  error of  $2.0 \mu\text{mol kg}^{-1}$  at low CFC concentrations can be regarded as cruise dependent. Most grid points are influenced by at least two cruises (e. g. a zonal and a meridional section). Thus the error of  $2.0 \mu\text{mol kg}^{-1}$  is divided by  $\sqrt{2}$  for each grid point and by  $\sqrt{n}$ , for the whole inventory, where  $n$  denotes the number of cruises.

For inventory differences of  $C_{\text{ant}}$  between times  $t_1$  and  $t_2$ , the errors due to a change in  $C_{\text{ant}}$  and CFC disequilibria and the  
325 errors due to uncertainties in the TTD shape only have to be applied to the portion of  $C_{\text{ant}}$  that is added between  $t_1$  and  $t_2$ . For the water formed prior to time  $t_1$ , which is still present at time  $t_2$ , these systematic errors mainly cancel out (Steinfeldt *et al.*, 2009).

When comparing the predicted  $C_{\text{ant}}$  values for time  $t_2$  based on observations at  $t_1$  with the  $C_{\text{ant}}$  values based directly on observations at  $t_2$ , the error due to a change in the  $C_{\text{ant}}$  disequilibrium is neglected. The reason is that here we are interested in  
330 the effect of a change in age on the  $C_{\text{ant}}$  concentrations and not in the effect of biogeochemical changes. Second, a change in the  $C_{\text{ant}}$  disequilibrium would effect the  $C_{\text{ant}}$  values for the prediction from observations at  $t_1$  and from more recent observations at  $t_2$  in a similar way.

### 3 Results and Discussion

#### 3.1 Basin-wide $C_{\text{ant}}$ distribution

335 The  $C_{\text{ant}}$  concentration and inventories of the Atlantic between  $70^\circ\text{S}$  and  $65^\circ\text{N}$  are computed for the reference years 1990, 2000, and 2010 from the decadal CFC/SF<sub>6</sub> data. In addition, we use all data to calculate a quasi climatological distribution of the Atlantic  $C_{\text{ant}}$  inventories, again referenced to 1990, 2000 and 2010. All inventories and their uncertainties are listed in Table 4. The Atlantic inventory of about  $55 \text{ Pg C}$  in 2010 makes up 38% global  $C_{\text{ant}}$  storage ( $143 \text{ Pg C}$ , “best estimate” in Khatiwala *et al.* (2013), whereas the fractional areal cover of the parts of the Atlantic considered here is only about 22%.

340 The climatological column inventory obtained from the extended TTD method (Fig. 6) reflects the general patterns reported in previous studies, which are based on different methods (Sabine *et al.* (2004):  $\Delta C^*$  method, Waugh *et al.* (2006): TTD method, Khatiwala *et al.* (2013): Green’s function method (GF)). Note that here, in contrast to Waugh *et al.* (2006), we use



**Table 4.** Atlantic  $C_{\text{ant}}$  inventories in Pg C for reference years 1990, 2000, and 2010 based on all tracer data and on tracer data from the decade centered around the reference year only.

	1990	2000	2010
	all data	all data	all data
North	$21.3 \pm 3.5$	$25.4 \pm 4.2$	$30.2 \pm 4.9$
South	$17.8 \pm 3.7$	$21.2 \pm 4.4$	$25.2 \pm 5.2$
Total	$39.1 \pm 7.2$	$46.6 \pm 8.5$	$55.4 \pm 10.1$
	data from 1982–1994	data from 1995–2005	data from 2006–2014
North	$21.3 \pm 3.6$	$25.4 \pm 4.2$	$30.3 \pm 4.9$
South	$18.3 \pm 4.1$	$21.0 \pm 4.4$	$24.3 \pm 4.6$
Total	$39.7 \pm 7.7$	$46.5 \pm 8.5$	$54.6 \pm 9.5$

TTDs with different  $\Delta/T$  ratios and include the dilution with old water. The maximum of the  $C_{\text{ant}}$  column inventory is located in the subpolar northwestern Atlantic. A tongue of high  $C_{\text{ant}}$  column inventories stretches southward from the  $C_{\text{ant}}$  maximum in the northwestern Atlantic towards the equator. This reflects the southward propagation of NADW, mainly within the DWBC (Rhein *et al.*, 2015). NADW is relatively high in  $C_{\text{ant}}$  compared to the deep water masses of southern origin.

The zonal mean sections for the eastern and western basin of the Atlantic shown in Fig. 7 highlight the vertical  $C_{\text{ant}}$  distribution and the contributions of the different water masses to the column inventory.  $C_{\text{ant}}$  concentrations are high at the surface and in the central waters formed in the subtropical gyres. The maximum is found at the surface in the tropical/subtropical zone, where SST is highest. The reason is that the  $C_{\text{ant}}$  equilibrium concentration increases with temperature and alkalinity. Especially the subtropical gyres show high values of salinity and also alkalinity (Lee *et al.*, 2006). The AAIW layer below forms a kind of transition zone between the  $C_{\text{ant}}$ -rich mode waters above and the  $C_{\text{ant}}$ -poor old deep waters below.

The most striking feature in the deep waters are the elevated  $C_{\text{ant}}$  concentrations in the North Atlantic (Fig. 7). They are highest in the western basin in the LSW layer, as this water mass is directly formed there (see section 2.2). The spreading time for DSOW from its origin in the Nordic Seas towards the Labrador Sea is about 5 yr (Rhein *et al.*, 2015), resulting in lower  $C_{\text{ant}}$  concentrations. The NADW component with the lowest  $C_{\text{ant}}$  values is the ISOW, as this water mass has the longest travel time into the western Atlantic via the Charlie-Gibbs Fracture Zone (Smethie and Swift, 1989). The northeastern Atlantic does in general exhibit smaller  $C_{\text{ant}}$  values in the deep waters. The LSW is also present there, but with lower concentrations due to the spreading time of around 5 yr from the formation region in the Labrador Sea towards the European continent (Sy *et al.*, 1997; Yashayaev *et al.*, 2007). The ISOW in the eastern basin does not reach the bottom of the deep basin, and the DSOW is not able to cross the Mid-Atlantic Ridge towards the east in the North Atlantic, so the deepest waters in the eastern basin (LDW) are low in  $C_{\text{ant}}$ . The southward spreading of NADW mainly in the DWBC leads to a tongue of enhanced  $C_{\text{ant}}$  concentrations



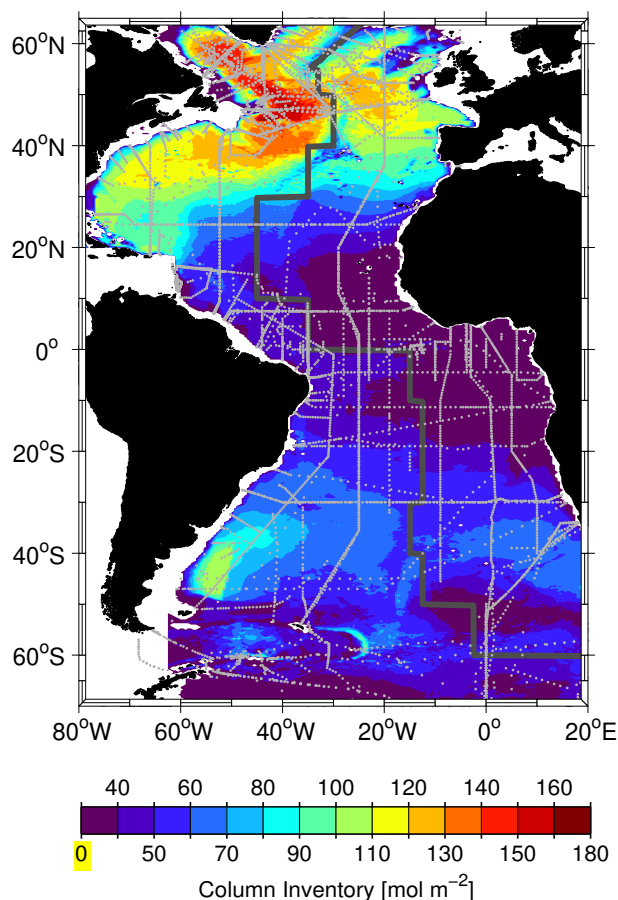


**Figure 6.** Map of the climatological  $C_{ant}$  column inventory referenced to 2010 based on all tracer data between 1982 and 2014. The thick line following the Mid-Atlantic Ridge indicates the boundary between eastern and western basin. Dots indicate the locations of tracer samples used for the  $C_{ant}$  calculation.

in the western basin which reaches south of the equator. The slightly enhanced concentrations in the LSW and AABW in the eastern equatorial Atlantic are due to the import of deep water from the western basin (Rhein and Stramma, 2005).

365 Also in the deep South Atlantic  $C_{ant}$  decreases from west to east. The higher  $C_{ant}$  concentrations in the west are due to the spreading of AABW, which propagates from the Weddell Sea northward into the deep basins of the western Atlantic (Orsi *et al.*, 1999). Another AABW branch continues eastward near 60°S. This branch can be seen in the enhanced  $C_{ant}$  values in Fig. 7a. It is also identified in the Prime Meridian Section in Huhn *et al.* (2013) by the deep CFC-12 maximum. Huhn *et al.* (2013) describe a second CFC-12 maximum that is related to the flow in opposite direction at the Antarctic continental slope  
370 between 3000 m and 4000 m depth. This feature does not show up here, as the slope does not follow a straight zonal line. Furthermore, it is partially located south of 70°S, which is outside the area considered here. In general, the  $C_{ant}$  concentrations

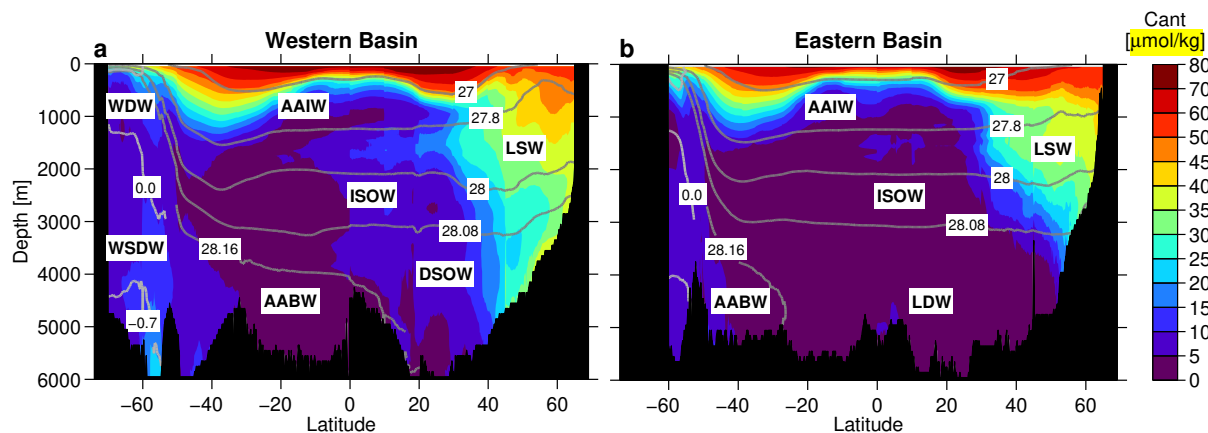


**Figure 7.** Zonal mean sections of  $C_{\text{ant}}$  referenced to 2010 based on all tracer data between 1982 and 2014. a: western basin, b: eastern basin. Contour lines are shown as in Fig. 2.

in the AABW core are considerably smaller compared to NADW. Through the entrainment of old WDW (see section 2.2), the transient tracer signal of AABW gets diluted, which explains the smaller  $C_{\text{ant}}$  values.

Overall, the improved TTD method used here leads to  $C_{\text{ant}}$  distributions that are compatible with the spreading of the water masses and the distribution of transient tracers that have been introduced into the ocean more recently. In contrast to that, the GF and the  $\Delta C^*$  method in *Khatriwala et al. (2013)* show very low  $C_{\text{ant}}$  values in the AABW. This is an unlikely scenario, as this water mass contains considerable amounts of CFCs (*van Heuven et al., 2011; Huhn et al., 2013*), which have been in the atmosphere for a shorter time than  $C_{\text{ant}}$ . The  $\Delta C^*$  method also gives low  $C_{\text{ant}}$  concentrations in deep waters, not only in the AABW, but also in the Overflow Waters (ISOW & DSOW) in the North Atlantic (*Vázquez-Rodríguez et al., 2009*).

Our results show a notable decadal increase in anthropogenic carbon over the period 1990–2010 both for the North and the South Atlantic. The temporal  $C_{\text{ant}}$  inventory changes ( $\Delta_t C_{\text{ant}}$ ) are given in Table 5 together with results from other studies.

The  $C_{\text{ant}}$  storage rate increases slightly from the first decade (1990–2000) to the second (2000–2010) for both hemispheres. The results from the other studies agree with ours within the error range except for the North Atlantic between 1990 and 2000. There, the value in *Woosley et al. (2016)* (adopted from *Wanninkhof et al. (2010)*) is considerably smaller ( $1.9 \pm 0.4$  Pg C compared to  $4.1 \pm 1.7$  Pg C in our study). Note that *Wanninkhof et al. (2010)* infer the  $C_{\text{ant}}$  change over the whole Atlantic from only one cruise which, in the North Atlantic, is located in the eastern basin and hence does not cover the deep water formation areas in the Irminger and Labrador Sea. This may introduce a bias in the results compared to our study. For the second period from 2000–2010, *Woosley et al. (2016)* use four cruises, also a small number compared to the amount of cruises/data used in this study. Nevertheless, the agreement for the second decade with *Woosley et al. (2016)* is good ( $4.9 \pm 1.8$  PG C vs.  $4.4 \pm 0.9$  Pg C).

By applying the eMLR( $C^*$ ) method to inorganic carbon observations obtained from the previous GLODAPv2 version, *Gruber et al. (2019)* report an increase in the Atlantic inventory between 1994 and 2007 of  $11.9 \pm 1.3$  Pg C. However, they



**Table 5.** Decadal changes in Atlantic  $C_{\text{ant}}$  inventories ( $\Delta_t C_{\text{ant}}$ , in Pg C). The inventory differences are obtained from the “decadal data only” inventories listed in Table 3. They are compared with the values given in *Woosley et al.* (2016) (based on the eMLR method, the  $C_{\text{ant}}$  increase from 1990 to 2000 in *Woosley et al.* (2016) is adopted from *Wanninkhof et al.* (2010), and the increase over the whole 1990–2010 period is the sum of both results), and *Gruber et al.* (2019) (eMLR( $C^*$ )).

	this study	<i>Woosley et al.</i> (2016)	<i>Gruber et al.</i> (2019)
1990–2000			
North	$4.1 \pm 1.7$	$1.9 \pm 0.4$	-
South	$2.7 \pm 2.2$	$3.2 \pm 0.7$	-
Total	$6.8 \pm 3.4$	$5.1 \pm 1.0$	-
2000–2010			
North	$4.9 \pm 1.8$	$4.4 \pm 0.9$	-
South	$3.2 \pm 2.3$	$3.7 \pm 0.8$	-
Total	$8.1 \pm 3.7$	$8.1 \pm 1.6$	-
1990–2010			
North	$9.0 \pm 2.8$	$6.3 \pm 1.0$	$9.2^a \pm 0.6$ ( $6.0 \pm 0.4^b$ )
South	$5.9 \pm 2.5$	$6.9 \pm 1.1$	$9.0^a \pm 1.8$ ( $5.9^b \pm 1.2$ )
Total	$14.9 \pm 4.1$	$13.2 \pm 1.9$	$18.2^a \pm 2.0$ ( $11.9^b \pm 1.3$ )

<sup>a</sup> value extrapolated to the period 1990–2010

<sup>b</sup> original value from *Gruber et al.* (2019) for the period 1994–2007

added 1.0 Pg C to the total deep Atlantic inventory below 3000 m that their method did not reproduce well. This added value is close to our findings with a  $C_{\text{ant}}$  increase of 1.1 Pg C below 3000 m between 1990 and 2010, which in our case is based directly on data. The total Atlantic  $C_{\text{ant}}$  storage in *Gruber et al.* (2019) is larger than our results when the value is expanded to the period 1990–2010 ( $14.9 \pm 4.1$  Pg C vs.  $18.2 \pm 2.0$  Pg C), and also higher than in *Woosley et al.* (2016) and the model study by *Clement and Gruber* (2018). The main differences to our  $C_{\text{ant}}$  storage occur in the South Atlantic (see Table 5).

### 3.1.1 Local $C_{\text{ant}}$ changes

### 3.2 $C_{\text{ant}}$ increase 1990–2010

We will now discuss the decadal  $C_{\text{ant}}$  changes between 1990 and 2010 in different regions/water masses of the Atlantic. Fig. 8 shows the mean annual storage rates for the respective decades between 1990 and 2010 and the total time period 1990–2010 over the whole water column (Fig. 8a, c, e) and the deep and bottom water layers only (Fig. 8b, d, f), which comprise the  $\sigma_{1.5}$  and  $\sigma_4$  layers from table S1. Fig. S3 shows the same  $C_{\text{ant}}$  changes as Fig. 8, but expressed as relative numbers. In Fig. 9 the changes in  $C_{\text{ant}}$  concentrations in the western and eastern basin are depicted. The  $C_{\text{ant}}$  increases shown in Fig. 8 and Fig. 9 reveal similar patterns as the  $C_{\text{ant}}$  distribution in Fig. 6 and Fig. 7, i.e. the  $C_{\text{ant}}$  increase over time is high where the



$C_{\text{ant}}$  concentration is also high. The largest increase appears close to the surface and in the subtropical mode waters, also the NADW contributes significantly to the Atlantic  $C_{\text{ant}}$  storage. This becomes particularly evident when comparing the column inventories for the whole water column (Fig. 7a, c, e) with those for the deep and bottom waters only (Fig. 8b, d, and f): In the subpolar North Atlantic, where the deep water layer reaches close to the surface, the  $C_{\text{ant}}$  storage in deep and bottom waters alone is almost as large as for the total water column. The southward propagation of NADW in the western basin is reflected by a significant  $C_{\text{ant}}$  increase that extends to  $10^{\circ}\text{S}$  and is most pronounced in the LSW layer (Fig. 9a, c and e). In the eastern basin, any noticeable spatial  $C_{\text{ant}}$  increase of the younger NADW layer (LSW and ISOW) is limited to the region north of  $30^{\circ}\text{N}$ .

The deep and bottom waters in the Atlantic that are not influenced by younger NADW mainly show insignificant  $C_{\text{ant}}$  changes. South of about  $40^{\circ}\text{S}$ , the AABW (including its precursors WSDW and WBW) exhibits a  $C_{\text{ant}}$  increase above the detection limit at least in some places, especially when considering the whole period from 1990 to 2010 (Fig. 9e, f). These also contribute to the increase in the column inventory of the deep and bottom waters south of  $40^{\circ}\text{S}$  shown in Fig. 8f. The differences between the decadal  $C_{\text{ant}}$  increase from 1990 to 2000 and from 2000 to 2010 will be discussed in section 3.3 on decadal variability.

### 3.2.1 Comparison of local $C_{\text{ant}}$ changes from the modified TTD method with dilution with other publications

We now compare our inferred local  $C_{\text{ant}}$  changes in the Atlantic with other published results. For the subpolar North Atlantic, the area with the highest increase in  $C_{\text{ant}}$  column inventory, *Pérez et al.* (2010) find similar storage rates ( $1.74\text{ mol m}^2\text{ yr}^{-1}$  in the Irminger Sea and  $1.88\text{ mol m}^2\text{ yr}^{-1}$  in the Iceland basin) as shown in Fig. 8, but only from 1991 to 1997, where the North Atlantic Oscillation (NAO) was in a high phase. Afterwards, in the low NAO period between 1997 and 2006, their rate is less than a quarter of the previous value ( $0.3 - 0.4\text{ mol m}^2\text{ yr}^{-1}$ ). Also for the northeastern Atlantic, *Pérez et al.* (2010) yield lower storage rates ( $0.72\text{ mol m}^2\text{ yr}^{-1}$  for 1981–2006) compared to our analyses ( $> 1.0\text{ mol m}^2\text{ yr}^{-1}$ , Fig. 8a, c, d). In contrast to *Pérez et al.* (2010), our results are averaged over a larger region and also a longer time period (a decade compared to six and nine years in *Pérez et al.* (2010) for the Irminger and Iceland basin), which may lead to a damping of sudden, regional changes in the  $C_{\text{ant}}$  storage. However, the low  $C_{\text{ant}}$  increase in *Pérez et al.* (2010) after 1997 also points to methodological differences between the  $\varphi C_{\text{T}}^0$  method used in *Pérez et al.* (2010) and the modified TTD method with dilution used here. A comparison of Fig. 9a and 9c indicates that in the decade 2000–2010 the  $C_{\text{ant}}$  storage in the deeper part of the LSW is indeed very small (due to a reduction in the convection depth). The other water masses, however, i. e. the Overflow Waters and the waters above 1000m, do not show a decrease in the  $C_{\text{ant}}$  uptake, in agreement with the ongoing renewal of these water masses. Thus, the small increase of the  $C_{\text{ant}}$  column inventory after 1997 in *Pérez et al.* (2010) seems to be unrealistic.

In the western South Atlantic the  $C_{\text{ant}}$  increase from our modified TTD method is similar to the results in *Ríos et al.* (2012) based on the  $\varphi C_{\text{T}}^0$ . The  $C_{\text{ant}}$  storage is highest in the Central Water, decreases downward with a minimum in the lower part of the NADW and shows some patches of significant  $C_{\text{ant}}$  increase towards the AABW near the bottom south of  $50^{\circ}\text{S}$  (Fig. 9e). In the Weddell gyre along the Prime Meridian, *van Heuven et al.* (2011) also find significant  $C_{\text{ant}}$  changes near the bottom. Applying the MLR method, they get an increase rate of  $0.445\text{ }\mu\text{mol kg}^{-1}$  per decade, whereas the trend of the directly



440 observed carbon data is  $1.15 \mu\text{mol kg}^{-1}$  per decade. The latter compares well with our  $C_{\text{ant}}$  increase of about  $1 - 2 \mu\text{mol kg}^{-1}$  per decade, Fig. 9e and 9f. *van Heuven et al.* (2011) do not provide a full explanation for the discrepancy between the directly observed carbon increase and that derived from the MLR method. They assume that the larger directly observed carbon trend could be probably ascribed to the increase of  $C_{\text{ant}}$ .

*Gruber et al.* (2019) find the highest increase of the  $C_{\text{ant}}$  column inventory between 1994 and 2007 in the subtropical North and South Atlantic. In the northern subtropics, their result is similar to our findings (Fig. 8), but larger than our values in the South Atlantic. These high storage rates in the southern subtropical Atlantic are the main reason for the higher Atlantic  $C_{\text{ant}}$  increase in *Gruber et al.* (2019) compared to our results (Table 5). On the other hand, the large maximum in the subpolar North Atlantic with storage rates up to  $2 \text{mol m}^{-2} \text{yr}^{-1}$  (Fig. 8) are not found in the study by *Gruber et al.* (2019), as the  $C_{\text{ant}}$  core in the overflow waters is missing there. The lack of  $C_{\text{ant}}$  at depth in *Gruber et al.* (2019) is compensated by a larger  $C_{\text{ant}}$  increase in the upper layers, mainly in the subtropical gyre (see Fig. 1 in *Gruber et al.* (2019)), so the  $C_{\text{ant}}$  storage for the whole North Atlantic in *Gruber et al.* (2019) is similar to ours (Table 5).

The best qualitative agreement with our results for the  $C_{\text{ant}}$  increase shows up in the model data of *Clement and Gruber* (2018). There, the maximum in the increase of the  $C_{\text{ant}}$  column inventory is located in the subpolar North Atlantic, with a tongue of high  $C_{\text{ant}}$  storage reaching towards the equator in the western basin (see Fig. 1c in *Clement and Gruber* (2018)). The minima are located along the African coast and in the Southern Ocean, as in our Fig. 8. Also the vertical structures of the  $C_{\text{ant}}$  distribution are similar, as can be seen from a comparison of Fig. 3d in *Clement and Gruber* (2018) with our Fig. 9.

### 3.3 Decadal variability of $C_{\text{ant}}$ storage

As mentioned above, the TTD technique in general allows to make predictions for  $C_{\text{ant}}$  concentrations based on older observations if one assumes a steady state ocean, i. e. the TTD  $\mathcal{G}$  remains constant with time. In this case, the  $C_{\text{ant}}$  increase with time is solely due to the rising atmospheric  $\text{CO}_2$ . The TTD method thus allows to distinguish between the  $C_{\text{ant}}$  variability generated by changes in oceanic circulation (which implies a change of the TTD) and the expected  $C_{\text{ant}}$  increase with time resulting merely from the atmospheric  $\text{CO}_2$  increase.

#### 3.3.1 Evolution of $C_{\text{ant}}$ for a steady state ocean

We will first consider the effect of the rising atmospheric  $\text{CO}_2$  on the oceanic  $C_{\text{ant}}$  concentrations. If the mixed layer concentration of the tracer  $C^0$  increases exponentially with time,  $C^0(t + \Delta t) = C^0(t) \exp(\lambda \Delta t)$ , then, following Eq. 1, the concentration of  $C$  in the ocean interior increases in the same way,  $C(\mathbf{x}, t + \Delta t) = C(\mathbf{x}, t) \exp(\lambda \Delta t)$ . *Steinfeldt et al.* (2009) applied an exponential fit of  $C_{\text{ant}}^0(t)$  for the time 1850–2003 and yielded a mean growing rate of  $1.69 \% \text{yr}^{-1}$ . Note that the increase rate of the equilibrium surface concentration  $C_{\text{ant}}^0(t)$  differs from the change of  $\text{CO}_2$  in the atmosphere due to the nonlinear carbon chemistry. Small deviations of  $C_{\text{ant}}^0(t)$  from the exponential fit cause the exact  $C_{\text{ant}}$  increase rate to depend both on the shape of the TTD (and thus the location) and the reference times for which  $C_{\text{ant}}$  is calculated. Here, we do not extend the exponential fit of  $C_{\text{ant}}^0(t)$  towards 2010, but infer mean decadal increase rates from the  $C_{\text{ant}}$  inventories in 1990, 2000, 2010 based on all CFC/SF<sub>6</sub> data (values in Table 3). The resulting increase is  $1.76 \% \text{yr}^{-1}$  for the decade 1990–2000 and  $1.75 \% \text{yr}^{-1}$  for 2000–



**Table 6.**  $C_{\text{ant}}$  accumulation anomalies for the Atlantic Ocean ( $\Delta_t C_{\text{ant}}^{\text{anom}}$ ), i. e. deviations between the  $C_{\text{ant}}$  increase based on tracer data from the actual period and the predicted  $C_{\text{ant}}$  increase based on tracer data from the previous period.

	$C_{\text{ant}}^{2000} - C_{\text{ant}}^{1990 \rightarrow 2000}$	$C_{\text{ant}}^{2010} - C_{\text{ant}}^{2000 \rightarrow 2010}$	$C_{\text{ant}}^{2010} - C_{\text{ant}}^{1990 \rightarrow 2010}$
North	$0.0 \pm 1.7$	$0.0 \pm 1.9$	$0.0 \pm 2.1$
South	$-0.8 \pm 2.2$	$-0.7 \pm 2.3$	$-1.7 \pm 2.6$
Total	$-0.8 \pm 3.5$	$-0.7 \pm 3.8$	$-1.6 \pm 4.4$

2010. Both values are quite close to the result of  $1.69\% \text{ yr}^{-1}$  in *Steinfeldt et al.* (2009). *Gruber et al.* (2019) also inferred an expected  $C_{\text{ant}}$  change based on the atmospheric  $\text{CO}_2$  increase and mean changes in the buffer factor and  $C_{\text{ant}}$  disequilibrium. The resulting  $C_{\text{ant}}$  change between 1994 and 2007 was 28%, or  $1.92\% \text{ yr}^{-1}$ . The higher value is probably because *Gruber et al.* (2019) considered only the atmospheric  $\text{CO}_2$  increase between 1994 and 2007, which is larger than a longer term mean, as the  $\text{CO}_2$  growth rate has increased. The  $C_{\text{ant}}$  increase of the older waters in the ocean interior, however, reflects the smaller rise of atmospheric  $\text{CO}_2$  from earlier decades.

### 3.3.2 Deviations of $C_{\text{ant}}$ storage from steady state

Here, we come back to the  $C_{\text{ant}}$  accumulation anomalies  $\Delta_t C_{\text{ant}}^{\text{anom}}$ , that have been introduced in section 2.3. The magnitude of these anomalies over the decades 1990–2000 and 2000–2010 as for the total 20 year period 1990–2010 is presented in Table 6. In the South Atlantic,  $\Delta_t C_{\text{ant}}^{\text{anom}}$  is slightly negative. This would imply a decrease in  $C_{\text{ant}}$  storage due to changes in circulation/ventilation. Note, however, that all numbers in Table 6 are not significantly different from zero. Thus, at least for the North and South Atlantic as a whole, the  $C_{\text{ant}}$  increase over the last 20 years is almost in agreement with the rising atmospheric  $\text{CO}_2$ . On smaller regional scales, however, there are regions where  $\Delta_t C_{\text{ant}}^{\text{anom}}$  is statistically significantly different from zero, especially for the 20 year period between 1990 and 2010 (Fig. 10). In general, the local extrema of  $\Delta_t C_{\text{ant}}^{\text{anom}}$  are about  $\pm 5 \mu\text{mol kg}^{-1}$ , the same magnitude as in (*Gruber et al.*, 2019).

The zonal mean section obtained for the western Atlantic for the period 1990–2010 (Fig. 10e) shows three larger scale dipole like structures. One is located in the South Atlantic, with negative  $C_{\text{ant}}$  anomalies south of  $40^\circ\text{S}$  around 1000m depth and a positive anomaly equatorward south of  $20^\circ\text{S}$  in a slightly shallower depth range. The negative anomaly is located in the density range of AAIW and below, the positive anomaly in the density range of AAIW and above (Subantarctic Mode Water, SAMW). This dipole structure has been inferred in *Waugh et al.* (2013) from transient tracer data for the southern parts of the Atlantic, Indian, and Pacific Ocean. These authors ascribe the changes in ventilation to a strengthening and southward movement of the westerly wind belt. This leads to enhanced upwelling of older water with low  $C_{\text{ant}}$  south of the polar front and increased northward Ekman transport and formation of mode waters (with high  $C_{\text{ant}}$ ) north of the front. A comparison of Fig. 10a, 10c, and 10e reveals that this anomaly mainly develops over the first decade considered here, i. e. between 1990 and 2000, thus it is might be an expression of decadal variability rather than a longterm trend. A similar dipole in the upper 1000m of the South





Atlantic is also evident in the study of Gruber *et al.* (2019). Tanhua *et al.* (2017) found a large  $C_{\text{ant}}$  storage in SAMW, at least between 1990 and 2005.

500 The second dipole is located in the northwestern tropical Atlantic with positive  $\Delta_t C_{\text{ant}}^{\text{anom}}$  around 500m and negative  $\Delta_t C_{\text{ant}}^{\text{anom}}$  close to the surface (Fig. 10e). This pattern might be interpreted as an intensification of the subtropical cell, with enhanced production and southward transport of  $C_{\text{ant}}$  rich mode water and also enhanced equatorial upwelling of older water low in  $C_{\text{ant}}$ . Such a change in the subtropical cell of the North Atlantic has been inferred from an inverse model in DeVries *et al.* (2017), however for the 1990s. Unfortunately, the study in DeVries *et al.* (2017) ends in 2010, and the decades in which  
505 the data are grouped are shifted by 5 years compared to our study, thus prohibiting a direct comparison of the decadal results. Different to our results, Gruber *et al.* (2019) find negative  $C_{\text{ant}}$  anomalies in the whole tropical Atlantic over the upper 1000m.

The northern most dipole of  $\Delta_t C_{\text{ant}}^{\text{anom}}$  is located north of 40°N in the subpolar North western Atlantic including the Labrador Sea (Fig. 9e). This structure reflects the observed variability of convective activity in the Labrador Sea, the associated changes in LSW formation and the relatively fast spreading of LSW in the subpolar North Atlantic. An unprecedented deep reaching  
510 convection formed a very dense mode of LSW from 1987 to 1994 (Yashayaev, 2007). During the following years, only lighter modes of LSW (Upper LSW, ULSW) have been formed (Stramma *et al.*, 2004; Kieke *et al.*, 2006; Yashayaev, 2007) whereas the pool of dense LSW (DLSW) has been exported from the formation region south- and eastward (Kieke *et al.*, 2007; Rhein *et al.*, 2015). These two processes are reflected in the positive  $\Delta_t C_{\text{ant}}^{\text{anom}}$  around 1000m (formation of ULSW modes) and the negative  $C_{\text{ant}}$  anomalies between 1500m and 2000m (export of DLSW) in Fig. 10c and 10e. This lack of  $C_{\text{ant}}$  storage in the  
515 deeper part of the LSW between 2000 and 2010 is also visible in Fig. 9c. In 2008, convection in the Labrador Sea exceeded a depth of 1600m again for the first time in years (Våge *et al.*, 2009), but without a great impact on the  $C_{\text{ant}}$  and oxygen trends (Rhein *et al.*, 2017). In the study by Gruber *et al.* (2019), the  $C_{\text{ant}}$  anomaly in the North Atlantic is negative down to a depth of  $\approx 2500\text{m}$  with the minimum in the upper  $\approx 1000\text{m}$ . Thus, a ULSW/DLSW dipole in  $C_{\text{ant}}$  is not found there. Studies about  
520 the convection in the Labrador Sea indicate that at least the upper 500 – 1000m of the water column have been convectively renewed every year since the 1990s (Yashayaev, 2007; Kieke and Yashayaev, 2015; Yashayaev and Loder, 2016), which makes a drastic decrease of the  $C_{\text{ant}}$  storage in that depth range unlikely. Starting in 2014, deep reaching convection in the Labrador Sea has re-emerged (Kieke and Yashayaev, 2015; Yashayaev and Loder, 2016). The most recent data from the Labrador Sea we use in this study date from 2013. We purposely excluded data from the following years in order to avoid mixing data from  
525 years of extremely deep versus years with shallower convection when calculating the mean value of the last decade. This gives a clearer picture of the consequences of less intense Labrador Sea convection on the  $C_{\text{ant}}$  concentrations. The  $C_{\text{ant}}$  signal from the enhanced convection since 2014 as reported in Fröb *et al.* (2016) and Rhein *et al.* (2017) thus does not show up in this study.

The positive value of  $\Delta_t C_{\text{ant}}^{\text{anom}}$  occurring in the deeper part of the LSW between 25°N and the equator (Fig. 10e) is also a consequence of the deep convection in the Labrador Sea around 1990. Parts of the  $C_{\text{ant}}$  rich waters formed during this time  
530 have been exported southward mainly in the Deep Western Boundary Current and arrived 8 years later at 26.5°N (Molinari *et al.*, 1998) and 10 to 13 years later at 16°N (Steinfeldt *et al.*, 2007; Rhein *et al.*, 2015). Fig. 10c and 10e show that these waters also have reached the equator based on the data from 2006 until 2014. Most of the data in the western equatorial Atlantic over



this period are from the GOSHIP lines A20 and A22 which were conducted in 2012. This indicates an upper boundary for the travel time from the Labrador Sea to the equator of 25 years, in agreement with previous studies (*Steinfeldt and Rhein, 2004*;  
535 *Rhein et al., 2015*).

In the bottom waters north of 40°N (DSOW) there is an alternating pattern of negative and positive  $\Delta_t C_{\text{ant}}^{\text{anom}}$  values (Fig. 9e). From 1965 to 2000, the overflow waters experienced a freshening trend lasting over more than three decades (*Dickson et al., 2002*). This long-term trend does not influence the  $C_{\text{ant}}$  uptake of ISOW and DSOW, as no such signal is evident in Fig. 10. Especially for the DSOW annual fluctuations in salinity (and also temperature) overlay the long-term freshening  
540 trend (*Yashayaev, 2007*). These different 'vintages' of DSOW might be the reason for the alternating minima and maxima in  $\Delta_t C_{\text{ant}}^{\text{anom}}$  in the bottom waters north of 40°N.

Another small region with a  $C_{\text{ant}}$  deficit is located within the bottom water (AABW) around 60°S. This is the area where the AABW originating from the Weddell Sea is advected eastward (see above). This recently ventilated AABW is relatively high  
in  $C_{\text{ant}}$  (Fig. 7a), but only shows a small decadal increase (Fig. 9e), lacking the expected growth from the atmospheric CO<sub>2</sub>.  
545 This result is in agreement with *Huhn et al. (2013)*, who also found an aging and  $\Delta_t C_{\text{ant}}^{\text{anom}}$  deficit of AABW in the Weddell Sea.

The  $\Delta_t C_{\text{ant}}^{\text{anom}}$  distribution over the eastern basin in Fig. 10b, d, and f has some similarities with the western part, i. e. the dipole structure in AAIW/SAMW in the South Atlantic and ULSW/DLSW in the northern part. In general, these features are less pronounced in the eastern Atlantic. The water mass formation regions are mainly located in the western Atlantic (as for  
550 LSW, DSOW, and also SAMW (*Čerovecki et al., 2013*)).  $\Delta_t C_{\text{ant}}^{\text{anom}}$  of these western newly formed waters becomes diluted when the anomalies spread eastward.

In the eastern subpolar North Atlantic, three other  $\Delta_t C_{\text{ant}}^{\text{anom}}$  signals are quite prominent. One negative anomaly around 50°N and 500 m, and two positive ones around 40°N and 55°N near 2500 m depth. The upper one in the density range of Subpolar Mode Water also appears in the western basin slightly further south. This anomaly might have similar reasons as the oxygen  
555 decline observed in this area. *Stendardo et al. (2015)* found a reduction in oxygen of the Central Waters along 47 – 48°N in the eastern basin and ascribed this to the penetration of oxygen depleted, and thus older, subtropical waters. The reason for the replacement of subpolar with subtropical waters was the contraction of the subpolar gyre between 1993 and 2002. As older waters are also lower in  $C_{\text{ant}}$ , we see a similar negative anomaly here for the decades after 1995.

The deeper positive  $\Delta_t C_{\text{ant}}^{\text{anom}}$  signal is located mainly in the density range of ISOW. Though the origin of this anomaly might  
560 be in the  $C_{\text{ant}}$  rich LSW formed around 1990. LSW spreads into the Iceland Basin, where it mixes with ISOW (*Yashayaev, 2007*). From there, the modified ISOW spreads back into the Labrador Sea (*Yashayaev, 2007*), but parts of it also continues southward in the eastern basin (*Fleischmann et al., 2001*), which might explain the positive  $C_{\text{ant}}$  anomaly there. Comparing figures 10b, d, and f indicates that the northern positive anomaly mainly occurs over the 1990–2000 period, and the southern over the second decade from 2000–2010. This underlines the assumptions that the DLSW formed between 1987 and 1994 is the  
565 reason for the positive  $C_{\text{ant}}$  anomaly, which then spreads southward. These ISOW signals are also reflected in the high increase of the  $C_{\text{ant}}$  column inventory over the deep water layer in the eastern North Atlantic between 1990 and 2000 (50°N–60°N) and, ten years later, further south at 40°N–50°N (Fig. 8b and d).



#### 4 Summary and Conclusions

We used a modified TTD method allowing for the admixture of old,  $C_{\text{ant}}$  free waters to access the  $C_{\text{ant}}$  inventory of the Atlantic, its increase and its variability over the last two decades. In 1990,  $39.7 \pm 7.7 \text{ Pg C}$  of  $C_{\text{ant}}$  were stored in the total Atlantic. Over the next 20 years, this amount increased to  $54.6 \pm 9.5 \text{ Pg C}$ . This increase is mainly caused by the rising atmospheric  $\text{CO}_2$  concentrations. Changes in circulation/ventilation have a regional impact on the  $C_{\text{ant}}$  concentrations, but only a minor effect on the basin wide inventory (a deficit of  $-1.6 \pm 4.4 \text{ Pg C}$  over 20 years).

The absolute  $C_{\text{ant}}$  inventories seem to be similar across the most common methods, like  $\Delta C^*$ , TTD and GF methods, except for some subregions like the Southern Ocean. Here, the incorporation of an explicit dilution into the TTD method leads to smaller  $C_{\text{ant}}$  concentrations which compare better to other methods like  $\Delta C^*$  and GF. Using the TTD method with a constant  $\Delta/\Gamma$  ratio and no dilution, *Waugh et al.* (2006) reduced their global  $C_{\text{ant}}$  inventory by 20 %, which they justified by a possible change in the  $\text{CO}_2$  disequilibrium. Using our TTD parameterization with variable  $\Delta/\Gamma$  ratios and including the dilution factor  $f$  leads to a reduction of the Atlantic  $C_{\text{ant}}$  inventory by almost 15 % (see Table 3). Thus, a systematic further downscaling does not seem to be necessary, and possible changes in the  $\text{CO}_2$  disequilibrium are contained in the error estimation. Greater discrepancies between the different  $C_{\text{ant}}$  calculation techniques occur in the vertical distribution of  $C_{\text{ant}}$ , especially regarding the  $C_{\text{ant}}$  fraction of the deep ocean. That has repercussions on the conclusions how well and how fast  $C_{\text{ant}}$  is stored in the ocean. Our decadal  $C_{\text{ant}}$  increments of  $6.8 \pm 3.4$  and  $8.1 \pm 3.7 \text{ Pg C}$  are about 30–40 % of the global values in *Friedlingstein et al.* (2020) of  $2.0 \pm 0.5$  and  $2.1 \pm 0.5 \text{ Pg C yr}^{-1}$ . The Atlantic area considered here makes up 22 % of the global ocean area. The high  $C_{\text{ant}}$  concentrations in the North Atlantic due to NADW formation lead to the high contribution of the Atlantic to the global  $C_{\text{ant}}$  storage compared to its volumetric fraction.

The main discrepancy between this study and others using the eMLR (*Woosley et al.*, 2016) and eMLR( $C^*$ ) method (*Gruber et al.*, 2019) is the regional distribution of the  $C_{\text{ant}}$  change. In the global study of *Gruber et al.* (2019), the increase of the  $C_{\text{ant}}$  column inventory in the Atlantic still exceeds that in the Pacific and Indian Ocean, but the global maximum in the North Atlantic is missing. This is due to a lack of the  $C_{\text{ant}}$  increase in recently ventilated NADW, especially the overflow waters. In order to account for that, *Gruber et al.* (2019) added an estimated  $C_{\text{ant}}$  storage in these waters of  $1 \text{ Pg C}$  between 1994 and 2010. Applying our TTD method, we find a  $C_{\text{ant}}$  increase also in the overflow waters and do not need such a correction. Also in *Woosley et al.* (2016) the deep layers of the North Atlantic are found to be almost stagnant in  $C_{\text{ant}}$ . The significant increase of the  $C_{\text{ant}}$  concentrations in ISOW and DSOW found in our study has not been reported before. Evident through the presence and temporal increase of CFCs in these overflow waters, it is unlikely that these waters have not contributed to the storage of  $C_{\text{ant}}$  over the last two decades.

Also the  $C_{\text{ant}}$  accumulation anomaly due to a variable ocean circulation in *Gruber et al.* (2019) opposes our findings. In *Gruber et al.* (2019), this anomaly is mainly positive in the South Atlantic, except for the AAIW layer, and negative in the North Atlantic. In our study, the deep South Atlantic shows a slightly negative  $C_{\text{ant}}$  accumulation anomaly, and in the north, we find alternating patterns with a positive anomaly in ULSW and negative in DLSW and SPMW. Using the standard TTDs



instead would even lead to a larger  $C_{\text{ant}}$  deficit in the South Atlantic (see Fig.3a–d) due to the higher “expected” CFC increase with time (Fig. 5).

The patterns of the  $C_{\text{ant}}$  accumulation anomalies found here mainly follow the changes in water mass age/ventilation that have already been described in previous studies, e. g. for the Southern Ocean (Waugh *et al.*, 2013; Huhn *et al.*, 2013), the  
605 reduced convective activity in the Labrador Sea (Kieke *et al.*, 2007; Yashayaev, 2007) and the export of well ventilated LSW towards the tropics/subtropics (Molinari *et al.*, 1998; Steinfeldt *et al.*, 2007; Rhein *et al.*, 2015). All these studies are based on the variability of hydrographic properties and/or anthropogenic tracers. The large  $C_{\text{ant}}$  accumulation anomaly in the old waters of the South Atlantic, as found in Gruber *et al.* (2019) is not reflected in hydrographic changes. It is also unlikely, as property anomalies in the ocean are typically large near the water mass formation regions and decay downstream towards the old waters  
610 in the ocean interior.

The investigation of oceanic circulation/ventilation variability and its impact on anthropogenic carbon storage is of importance for both the understanding of the mechanisms of the recent variability in oceanic carbon uptake (DeVries *et al.*, 2019) and the estimation of the future evolution of the oceanic carbon sink in a changing climate. In the future, also changes in the biogenic carbon or carbon/climate feedbacks, i. e. outgassing of  $\text{CO}_2$  in a warming ocean may play a larger role. Our results  
615 show that a decoupling of the atmospheric  $C_{\text{ant}}$  increase and the increase in the Atlantic  $C_{\text{ant}}$  storage has not yet been achieved by the observed decadal variability in water mass ventilation and circulation. A more permanent ventilation decrease of the major deep and bottom waters, **effective over several decades**, is likely needed to affect this relationship.

*Data availability.* Data are available at [https://www.nodc.noaa.gov/ocads/oceans/GLODAPv2\\_2019/\(GLODAPv2.2019\)](https://www.nodc.noaa.gov/ocads/oceans/GLODAPv2_2019/(GLODAPv2.2019)) and  
<https://www.bodc.ac.uk/geotraces/data/idp2017/> (GEOTRACES section GA02). The data of the additional cruises are available via PAN-  
620 GAEA  
(PE278: <https://doi.pangaea.de/10.1594/PANGAEA.911248>,  
SUBPOLAR08: <https://doi.pangaea.de/10.1594/PANGAEA.911310>,  
M82/2: <https://doi.pangaea.de/10.1594/PANGAEA.911301>,  
MSM21/2: <https://doi.pangaea.de/10.1594/PANGAEA.910957>,  
625 MSM27: <https://doi.pangaea.de/10.1594/PANGAEA.911225>,  
MSM28: <https://doi.pangaea.de/10.1594/PANGAEA.911234>,  
MSM38: <https://doi.pangaea.de/10.1594/PANGAEA.911240>,  
MSM39: <https://doi.pangaea.de/10.1594/PANGAEA.911243>).

## Appendix A: Vertical/Isopycnal Interpolation of Profiles

630 For the isopycnal interpolation of salinity, potential temperature and anthropogenic carbon, at each profile mean values over 38 density layers are calculated. The boundaries of these density intervals are given in table S1. For the upper layers, the potential density referenced to the surface is used ( $\sigma_\theta$ ), for the intermediate layers  $\sigma_{1.5}$ , referenced to 1500 dbar, and for the deep layers



**Table A1.** Boundaries of density layers and assumed saturation for CFCs and SF<sub>6</sub> in every layer.

	density [kgm <sup>-3</sup> ]	CFC/SF <sub>6</sub> - saturation [%]		density [kgm <sup>-3</sup> ]	CFC/SF <sub>6</sub> - saturation [%]		density [kgm <sup>-3</sup> ]	CFC/SF <sub>6</sub> - saturation [%]
$\sigma_\theta$	0	100	$\sigma_\theta$	27.6	95	$\sigma_{1.5}$	34.77	80
$\sigma_\theta$	24	100	$\sigma_{1.5}$	34.42	92.5	$\sigma_4$	45.8	80
$\sigma_\theta$	25	100	$\sigma_{1.5}$	34.5	90	$\sigma_4$	45.83	80
$\sigma_\theta$	25.5	100	$\sigma_{1.5}$	34.55	87.5	$\sigma_4$	45.86	80
$\sigma_\theta$	26	100	$\sigma_{1.5}$	34.6	85	$\sigma_4$	45.88	80
$\sigma_\theta$	26.5	100	$\sigma_{1.5}$	34.625	85	$\sigma_4$	45.9	80
$\sigma_\theta$	26.8	97.5	$\sigma_{1.5}$	34.65	85	$\sigma_4$	45.925	80
$\sigma_\theta$	27	95	$\sigma_{1.5}$	34.675	85	$\sigma_4$	45.95	80
$\sigma_\theta$	27.15	95	$\sigma_{1.5}$	34.7	82.5	$\sigma_4$	45.975	80
$\sigma_\theta$	27.3	95	$\sigma_{1.5}$	34.725	80	$\sigma_4$	46	80
$\sigma_\theta$	27.4	95	$\sigma_{1.5}$	34.75	80	$\sigma_4$	46.025	80
$\sigma_\theta$	27.5	95	$\sigma_{1.5}$	34.77		$\sigma_4$	46.95	80
$\sigma_\theta$	27.6					$\sigma_4$	46.1	80
						$\sigma_4$	46.15	80
						$\sigma_4$	46.2	80
						$\sigma_4$	50	80

$\sigma_4$ , referenced to 4000 dbar. At some locations, the deepest  $\sigma_\theta$  layer is located below the upper  $\sigma_{1.5}$  layers. In this case, these upper  $\sigma_{1.5}$  layers remain empty. The same holds for the transition between  $\sigma_{1.5}$  and  $\sigma_4$ . A mean value for a density layer is only calculated, if at least one data point is located within that density interval. Typically, the number of density levels for a deep reaching profile is about 30. The layers with the lightest densities only exist at low latitudes, and the densest  $\sigma_4$  layers only in the AABW core and in the North Atlantic south of Denmark Strait. The number of available samples from the water bottles is typically around 20 per profile, i. e. some density layers might not get assigned a mean value. As these “empty” layers change from profile to profile, there are still enough points for each density layer to perform the gridding procedure.

Only the bottle data from GLODAP have been used to calculate the layer thicknesses. One reason is that in GLODAP, also salinity and thus density are quality controlled. We calculated the difference between the layer thicknesses inferred from CTD and bottle data for a cruise where both are available. The root-mean-square error of the layer thicknesses is about 40m. If one assumes a maximal  $C_{\text{ant}}$  difference over this depth range of about  $20 \mu\text{mol kg}^{-1}$  (from Fig. 6), the difference in the  $C_{\text{ant}}$  column inventory would be  $\approx 40 \text{ m} \cdot 20 \mu\text{mol kg}^{-1} \cdot 1000 \text{ kg m}^{-3} = 0.8 \text{ mol m}^{-2}$ . That is about 1% of the total  $C_{\text{ant}}$  column inventory (see Fig. 5, between 30 and  $180 \text{ mol m}^{-2}$ ). The error of the layer thicknesses is randomly (in some cases the layer with the higher  $C_{\text{ant}}$  concentration is too thick, in other cases too thin). Due to the large number of profiles ( $> 1000$ ), the total error is much smaller than 1%.



## Appendix B: CFC and SF<sub>6</sub> saturation

The CFC and SF<sub>6</sub> saturations assumed for the different density layers are given in Table A1. They decrease from 100% in  
650 the upper waters to 80% in deep waters. For most cruises, the surface is close to saturation, both for CFCs and SF<sub>6</sub>. Hence,  
a saturation of 100% for the upper layers seems to be reasonable. For the deep layers, the saturation of the surface waters at  
the time of deep water formation, i. e. late winter/early spring needs to be known. Most cruises from higher latitudes, however,  
are from late spring until autumn, avoiding the severe winter conditions. In order to estimate the saturation of newly formed  
North Atlantic Deep Water, Fig. B1 shows the CFC-12 and SF<sub>6</sub> data from the western subpolar North Atlantic (Labrador Sea  
655 and Irminger Sea respectively) below 500 m depth for two different years, expressed as saturation with respect to the solubility  
equilibrium. This has been calculated by using the observed pot. temperature, salinity, and the atmospheric tracer concentration  
from the year of observation. Waters with the highest saturation may be interpreted as remnants from the last winter convection,  
waters with lower saturations are a mixture of recently ventilated and older water. In 1994, mainly the denser mode of LSW has  
been ventilated, between  $\sigma_{1.5} = 34.65 \text{ kg m}^{-3}$  and  $\sigma_{1.5} = 34.7 \text{ kg m}^{-3}$ . In 2013, the ventilation only reached densities above  
660  $\sigma_{1.5} = 34.6 \text{ kg m}^{-3}$ . The highest saturations in the ventilated density range are between 80% and 100% for both years. The  
SF<sub>6</sub> saturation in 2013 is only slightly below the values for CFC-12.

The overflow waters are not directly formed in the subpolar North Atlantic, but originate from the Nordic Seas. However, they  
are modified after passing the Greenland-Scotland-Ridge, e. g. the ISOW entrains Labrador Sea Water and Northeast Atlantic  
Water (*LeBel et al.*, 2008), and the DSOW warm and saline Atlantic Water and fresher water from the East Greenland Current  
665 (*Jochumsen et al.*, 2015). The tracer saturation of the overflow waters ( $\sigma_4 > 45.8 \text{ kg m}^{-3}$ ) in the Irminger Sea, downstream  
of the entrainment, are shown in Fig. B1 for data prior and after the year 2000. The saturation is even higher for the earlier  
period, probably due to short-term variability of the properties of the overflow waters (*Yashayaev*, 2007; *Jochumsen et al.*,  
2015). The maximum is around 80%, but most data points have a smaller saturation. Note, however, that the Irminger Sea is  
located downstream of the formation area, hence the overflow waters there is not newly formed, but has already been subject to  
670 aging and dilution, which reduces the apparent CFC saturation. In Fig. S1 also the tracer saturation from Table S1 is depicted,  
including the assumed error of 10%. The saturation of 85% for the major part of the LSW density range is identical with the  
value used in *Kieke et al.* (2006), *Kieke et al.* (2007), *Steinfeldt et al.* (2009). For the DSOW, the applied saturation of 80% is  
significantly larger than the 65% from *Steinfeldt et al.* (2009) but close to the value of 75% from *Swift et al.* (1980), *LeBel et*  
*al.* (2008).

## 675 Appendix C: Variation of TTD Parameters

The effect of the choice of the TTD parameters on the shape of the TTD and the inferred  $C_{\text{ant}}$  concentration is illustrated in  
Fig. C1 and Table C1. We assume a CFC-12 concentration of  $0.5 \text{ pmol kg}^{-1}$  observed in 2010, a CFC-saturation of 0.85, a  
potential temperature of  $\theta = 3^\circ\text{C}$  and a salinity of  $S = 34.9$ .  $C_{\text{ant}}$  is calculated for the reference year 2010 and an alkalinity of  
 $2308 \text{ } \mu\text{mol kg}^{-1}$  (the value derived from *Lee et al.* (2006) for the North Atlantic). The maximum of the TTD occurs at younger  
680 ages for  $\Delta/\Gamma = 2$  compared to the case with  $\Delta/\Gamma = 1$ . This is a quite general behaviour, i. e. increasing the  $\Delta/\Gamma$  ratio leads





**Table C1.** TTD parameters derived for a CFC-12 concentration of  $0.2 \text{ pmol kg}^{-1}$  in 2010, assuming a CFC-saturation of 0.85, a potential temperature of  $\theta = 3^\circ\text{C}$  and a salinity of  $S = 34.9$ .  $C_{\text{ant}}$  is calculated for the reference year 2010 and an alkalinity of  $2308 \text{ } \mu\text{mol kg}^{-1}$  (the value derived from *Lee et al., 2006* for the North Atlantic). Also given is the fraction of water older than 200 yr.

	$\Gamma$ [yr]	$\Delta$ [yr]	$C_{\text{ant}}$ [ $\text{pmol kg}^{-1}$ ]	$f > 200 \text{ yr}$
$\Delta/\Gamma = 1 \text{ } f = 1$	154.5	154.5	15.8	0.21
$\Delta/\Gamma = 2 \text{ } f = 1$	472	944	14.3	0.34
$\Delta/\Gamma = 1 \text{ } f = 0.5$	$82^a$	$82^a$	12.0	$0.10^a$

<sup>a</sup>Values are for the young TTD component only.

to a younger age of the mode of the TTD. Reducing the fraction of young water leads to an even younger mode, although in this case the  $\Delta/\Gamma$  ratio is always chosen as one. The younger the mode of the possible TTDs derived from a given CFC-12 concentration, the smaller is the inferred  $C_{\text{ant}}$  concentration (see Table C1).

The TTD  $\mathcal{G}_{\text{young}}$  for the young water in Figure S2 only represents half of the water, as the fraction  $f$  in this example equals 0.5. To illustrate how the complete TTD might look like, we assume an old TTD  $\mathcal{G}_{\text{old}}$  with  $\Gamma = 500 \text{ yr}$  and  $\Delta = 250 \text{ yr}$ . The sum of  $\mathcal{G}_{\text{young}}$  and  $\mathcal{G}_{\text{old}}$  is shown as dashed line in Figure S1. This choice of the parameters for  $\mathcal{G}_{\text{old}}$  is arbitrary, but it fulfills the condition that the inferred  $C_{\text{ant}}$  concentration is small ( $< 0.5 \text{ } \mu\text{mol kg}^{-1}$  in this case) and thus might be neglected. The sum of  $\mathcal{G}_{\text{young}}$  and  $\mathcal{G}_{\text{old}}$  only has one clear maximum. The mode of  $\mathcal{G}_{\text{old}}$  is much less pronounced than that of  $\mathcal{G}_{\text{young}}$ , so the complete TTD has a kind of saddle point around the mode of  $\mathcal{G}_{\text{old}}$  (250 yr in the example in Figure C1).

#### 690 Appendix D: Relative $C_{\text{ant}}$ change ( $\Delta_t C_{\text{ant}}$ ) between 1990 and 2010

*Author contributions.* R.S. carried out the calculations of anthropogenic carbon and prepared the manuscript with contributions from both coauthors.

*Competing interests.* The authors declare that they have no conflict of interest.

*Acknowledgements.* We thank the captains, crews and scientific participants of the numerous research cruises whose data have contributed to this work. The cruises SUBPOLAR08, M82/2, M85/1, MSM21/2, MSM27, MSM28, MSM38, and MSM39 have been conducted in the framework of programs funded by the German Federal Ministry for Education and Research (BMBF) (Cooperative Projects “Nordatlantik” and “RACE” (grants 03F0443C, 03F0605C and 03F0651C to M. Rhein)). K. Bulsiewicz (IUP at University of Bremen) measured the CFC and  $\text{SF}_6$  samples obtained from the cruises conducted by IUP Bremen. M. Rhein received funding from the German Research Foundation (DFG, grants RH 25/36-1, RH 25/36-2, and RH 25/36-3).



## 700 References

- Álvarez, M., Pérez, F., Bryden, H. L., and Ríos, A.: Physical and biogeochemical transports structure in the North Atlantic subpolar gyre, *J. Geophys. Res.: Oceans*, 109, C03027, <https://doi.org/10.1029/2003JC002015>, 2004.
- Brambilla, E. & Talley, L. D. (2008). Subpolar Mode Water in the northeastern Atlantic: 1. Averaged properties and mean circulation. *J. Geophys. Res.: Oceans*, 113, C04025, <https://doi.org/10.1029/2006JC004062>
- 705 Bullister, J., Rhein, M., and Mauritzen, C.: Deep Water Formation. In: *Ocean Circulation and Climate - Observing and Modelling the Global Ocean*, second edition, edited by G. Siedler, J. Church, J. Gould and S. Griffies, Academic Press, Oxford, ISBN 978-0-12-391851-2, 2013.
- Človečki, I., Talley, L. D., Mazloff, M. R. and Maze, G.: Subantarctic Mode Water Formation, Destruction, and Export in the Eddy-Permitting Southern Ocean State Estimate. *J. Phys. Oceanogr.*, 43(7), 1485–1511, <https://doi.org/10.1175/JPO-D-12-0121.1>, 2013.
- Clement, D., and Gruber, N.: The eMLR(C\*) method to determine decadal changes in the global ocean storage of anthropogenic CO<sub>2</sub>,  
710 *Global Biogeochem. Cy.*, 32, 654–679, <https://doi.org/10.1002/2017GB005819>, 2018.
- DeVries, T., Holzer, M., and Primeau, F.: Recent increase in oceanic carbon uptake driven by weaker upper-ocean overturning, *Nature*, 542, 215–218, <https://doi.org/10.1038/nature21068>, 2017.
- DeVries, T., Le Quéré, C., Andrews, O., Berthet, S., Hauck, J., Ilyina, T., Landschützer, Lenton, A., Lima, I. D., Nowicki, M., Schwinger, J., and Roland Séférian, R.: Decadal trends in the ocean carbon sink, *PNAS*, 116(24), 11646–11651,  
715 <https://doi.org/10.1073/pnas.1900371116>, 2019.
- Dickson, B., Yashayaev, I., Meincke, J., Turrell, B., Dye, S., and Holfort, J.: Rapid freshening of the deep North Atlantic Ocean over the past four decades, *Nature*, 416, 832–837, <https://doi.org/10.1038/416832a>. 2002.
- Fischer, J., Rhein, M., Schott, F. and Stramma, L.: Deep water masses and transports in the Vema Fracture Zone, *Deep-Sea Res. I*, 43(7) 1067–1074, [https://doi.org/10.1016/0967-0637\(96\)00044-1](https://doi.org/10.1016/0967-0637(96)00044-1), 1996.
- 720 Fleischmann, U., Hildebrandt, H., Putzka, A. and Bayer, R.: Transport of newly ventilated deep water from the Iceland Basin to the West European Basin, *Deep-Sea Res. I*, 48(8) 1793–1819, [https://doi.org/10.1016/S0967-0637\(00\)00107-2](https://doi.org/10.1016/S0967-0637(00)00107-2), 2001.
- Friedlingstein, P. et al. (2020). Global Carbon Budget 2020, *Earth Syst. Sci. Data*, 12, 3269–3340, <https://doi.org/10.5194/essd-12-3269-2020>, 2020.
- Friis, K., Körtzinger, A., Pätsch, J., and Wallace, D.: On the temporal increase of anthropogenic CO<sub>2</sub> in the subpolar North Atlantic, *Deep-Sea Res. I*, 52(5), 681–698, <https://doi.org/10.1016/j.dsr.2004.11.017>, 2005.
- 725 Fröb, F., Olsen, A., Våge, K., Moore, G. W. K., Yashayaev, Y., Jeansson, E. and Rajasakaren, B.: Irminger Sea deep convection injects oxygen and anthropogenic carbon to the ocean interior, *Nat. Commun.*, 7, 13244, <https://doi.org/10.1038/ncomms13244>, 2016.
- Gruber, N., Sarmiento, J. L., and Stocker, T. F.: An improved method for detecting anthropogenic C<sub>2</sub> in the oceans, *Global Biogeochem. Cy.*, 10(4), 809–837, <https://doi.org/10.1029/96GB01608>, 1996.
- 730 Gruber, N., Clement, D., Carter, B. R., Feely, R. A., van Heuven, S., Hoppema, M. et al.: The oceanic sink for anthropogenic CO<sub>2</sub> from 1994 to 2007, *Science*, 363, 1193–1199, doi: 10.1126/science.aau5153, 2019.
- Hall, T. M., Haine, T. W. N., and Waugh, D. W.: Inferring the concentration of anthropogenic carbon in the ocean from tracers, *Global Biogeochem. Cy.*, 16(GB1131), <https://doi.org/10.1029/2001GB001835>, 2002.
- Heinze, C., Meyer, S., Goris, N., Anderson, L., Steinfeldt, R., Chang, N., Le Quéré, C., and Bakker, D. C. E.: The ocean carbon sink –  
735 impacts, vulnerabilities and challenges, *Earth Syst. Dynam.*, 6, 327–358, <https://doi.org/10.5194/esd-6-327-2015>, 2015.
- Holzer, M., and Hall, T. M.: Transit-time and tracer age distributions in geophysical flows, *J. Atmos. Sci.*, 57, 3539–3558, 2000.



- Huhn, O., Rhein, M., Hoppema, M., and van Heuven, S.: Decline of deep and bottom water ventilation and slowing down of anthropogenic carbon storage in the Weddell Sea, 1984–2011, *Deep-Sea Res. I*, 76, 66–84, <https://doi.org/10.1016/j.dsr.2013.01.005>, 2013.
- 740 Iudicone, D., Speich, S., Gurvan, M. and Blanke, B.: The Global Conveyor Belt from a Southern Ocean Perspective, *J. Phys. Oceanogr.*, 38, 1401–1425, <https://doi.org/10.1175/2007JPO3525.1>, 2008.
- Jochumsen, K., Köllner, M., Quadfasel, D., Dye, S., Rudels, B., and Valdimarsson, H.: On the origin and propagation of Denmark Strait overflow water anomalies in the Irminger Basin, *J. Geophys. Res.: Oceans*, 120, 1841–1855, <https://doi.org/10.1002/2014JC010397>, 2015.
- 745 Khatiwala, S., Tanhua, T., Mikaloff Fletcher, S., Gerber, M., Doney, S. C., Graven, H. D., Gruber, N., McKinley, G. A., Murata, A., and Sabine, C. L.: Global storage of anthropogenic carbon, *Biogeosciences*, 10, 2169–2191, <https://doi.org/10.5194/bg-10-2169-2013>, 2013.
- Kieke, D., Rhein, M., Stramma, L., Smethie Jr., W. M., LeBel, D. A., and Zenk, W.: Changes in the CFC inventories and formation rates of Upper Labrador Sea Water, 1997–2001, *J. Phys. Oceanogr.*, 36(1), 64–86, <https://doi.org/10.1175/JPO2814.1>, 2006.
- Kieke, D., Rhein, M., Stramma, L., Smethie Jr., W. M., Bullister, J. L., and LeBel, D. A.: Changes in the pool of Labrador Sea Water in the subpolar North Atlantic, *Geophys. Res. Lett.*, 34, L06605, <https://doi.org/10.1029/2006GL028959>, 2007.
- 750 Kieke, D., and Yashayaev, I.: Studies of Labrador Sea Water formation and variability in the subpolar North Atlantic in the light of international partnership and collaboration, *Prog. Oceanogr.*, 132(3), 220–232, <https://doi.org/10.1016/j.pocean.2014.12.010>, 2015.
- Klatt, O., Roether, W., Hoppema, M., Bulsiewicz, K., Fleischmann, U., Rodehacke, C., Fahrbach, R., Weiss, R. F., and Bullister, J. L.: Repeated CFC sections at the Greenwich Meridian in the Weddell Sea, *J. Geophys. Res.: Oceans*, 107(C4), 3030, <https://doi.org/10.1029/2000JC000731>, 2002.
- 755 Lazier, J., Hendry, R., Clarke, A., Yashayaev, I., and Rhines, P.: Convection and restratification in the Labrador Sea, 1990–2000. *Deep-Sea Res. I*, 49(10), 1819–1835, [https://doi.org/10.1016/S0967-0637\(02\)00064-X](https://doi.org/10.1016/S0967-0637(02)00064-X), 2002.
- Lebel, D. A., Smethie Jr., W. M., Rhein, M., Kieke, D., Fine, R. A., Bullister, J. L., Min, D. H., Roether, W., Weiss, R., Andrié, C., Smythe-Wright, D., and Jones, E. P.: The formation rate of North Atlantic Deep Water and Eighteen Degree Water calculated from CFC-11 inventories observed during WOCE, *Deep-Sea Res. I*, 55(8) 901–910, <https://doi.org/10.1016/j.dsr.2008.03.009>, 2008.
- 760 Le Bras, I. A., Yashayaev, I., and Toole, J. M.: Tracking Labrador Sea Water property signals along the Deep Western Boundary Current, *J. Geophys. Res.: Oceans*, 122, 5348–5366, <https://doi.org/10.1002/2017JC012921>, 2017.
- Lee, K., Tong, L. T., Millero, F. J., Sabine, C. L., Dickson, A. G., Goyet, C., Park, G. H., Wanninkhof, R., Feely, R. A., and Key, R. M.: Global relationships of total alkalinity with salinity and temperature in surface waters of the world’s oceans, *Geophys. Res. Lett.*, 33, L19605, <https://doi.org/10.1029/2006GL027207>, 2006.
- 765 Mauritzen, C., Price, J., Sanford, T., and Torres, D.: Circulation and mixing in the Faroese Channels, *Deep Sea Res., Part I*, 52(6), 883–913, <https://doi.org/10.1016/j.dsr.2004.11.018>, 2005.
- McCartney, M. S.: The subtropical recirculation of mode waters, *J. Mar. Res.*, 40, 427–464, 1982.
- McCartney, M. S.: Recirculating components to the deep boundary current of the northern North Atlantic, *Prog. Oceanogr.*, 29, 283–383, [https://doi.org/10.1016/0079-6611\(92\)90006-L](https://doi.org/10.1016/0079-6611(92)90006-L), 1992.
- 770 Mercier, H., and Morin, P.: Hydrography of the Romanche and Chain Fracture Zones, *J. Geophys. Res.: Oceans*, 102, C5, 10373–10389, <https://doi.org/10.1029/97JC00229>, 1997.
- Molinari, R. L., Fine, R. A., Wilson, W. D., Curry, R. G., Abell, J., and McCartney, M. S.: The arrival of recently formed Labrador Sea Water in the Deep Western Boundary Current at 26.5°N. *Geophys. Res. Lett.*, 25(13), 2249–2252, 1998.



- Olsen, A., Lange, N., Key, R. M., Tanhua, T., Álvarez, M., Becker, S., et al: GLODAPv2.2019 – an update of GLODAPv2, *Earth Syst. Sci. Data*, 11, 1437–1461, <https://doi.org/10.5194/essd-11-1437-2019>, 2019.
- 775 Orsi, A. H., Johnson, G. C., and Bullister, J. L.: Circulation, mixing, and production of Antarctic Bottom Water, *Prog. Oceanogr.*, 43, 55–109, [https://doi.org/10.1016/S0079-6611\(99\)00004-X](https://doi.org/10.1016/S0079-6611(99)00004-X), 1999.
- Pérez, F. F., Vázquez-Rodríguez, M., Mercier, H., Velo, A., Lherminier, P., and Ríos, A. F.: Trends of anthropogenic CO<sub>2</sub> storage in North Atlantic water masses, *Biogeosciences* 7, 1789–1807, <https://doi.org/10.5194/bg-7-1789-2010>, 2010.
- 780 Pérez, F. F., Mercier, H., Vázquez-Rodríguez, M., Lherminier, P., Velo, A., Pardo, P. C., Roson, G., and Ríos, A. F.: Atlantic Ocean CO<sub>2</sub> uptake reduced by weakening of the meridional overturning circulation, *Nature Geoscience*, 6(2), 146–152, <https://doi.org/10.1038/ngeo1680>, 2013.
- Petit, T., Mercier, H., and Thierry, V.: First direct estimates of volume and water mass transports across the Reykjanes Ridge, *J. Geophys. Res.: Oceans*, 123, 6703–6719, <https://doi.org/10.1029/2018JC013999>, 2018.
- 785 Polzin, K. L. Toole, J. M., Ledwell, J. R., and Schmitt, R. W.: Spatial variability of turbulent mixing in the abyssal ocean, *Science*, 276, 93–96, 1997.
- Rhein, M., and Stramma, L.: Seasonal fluctuations in the Deep Western Boundary Current around the eastern tip of Brazil. *Deep-Sea Res. I*, 52(8), 1414–1428, <https://doi.org/10.1016/j.dsr.2005.03.004>, 2005.
- Rhein, M., Kieke, D., and Steinfeldt, R.: Ventilation of the Upper Labrador Sea Water, 2003–2005, *Geophys. Res. Lett.*, 34, L06603, doi:10.1029/2006GL028540, 2007. *Deep-Sea Res. I*, 52(8), 1414–1428.
- 790 Rhein, M., Kieke, D., and Steinfeldt, R.: Advection of North Atlantic Deep Water from the Labrador Sea to the southern hemisphere, *J. Geophys. Res.: Oceans*, 120, 2471–2487, <https://doi.org/10.1002/2014JC010605>, 2015.
- Rhein, M., Steinfeldt, R., Kieke, D., Stendardo, I., and Yashayaev, I.: Ventilation variability of Labrador Sea Water and its impact on oxygen and anthropogenic carbon, *Phil. Trans. R. Soc. A* 375(2102), <https://doi.org/10.1098/rsta.2016.0321>, 2017.
- 795 Rhein, M., Steinfeldt, R., Huhn, O., Sültenfuß, J., and Breckenfelder, T.: Greenland submarine melt water observed in the Labrador and Irminger Sea, *Geophys. Res. Lett.*, 45, 10.570-10.578, <https://doi.org/10.1029/2018GL079110>, 2018.
- Ríos, A. F., Velo, A., Pardo, P. C., Hoppema, M., and Pérez, F. F.: An update of anthropogenic CO<sub>2</sub> storage rates in the western South Atlantic basin and the role of Antarctic Bottom Water, *J. Mar. Sys.*, 94, 197–203, <https://doi.org/10.1016/j.jmarsys.2011.11.023>, 2012.
- Sabine, C. L., Feely, R. A., Gruber, N., Key, R. M., Lee, K., Bullister, J. L., R. Wanninkhof, Wong, C. S., Wallace, D. W. R., Tilbrook, B., 800 Millero, F. J., Peng, T. H., Kozyr, A., Ono, T., and Rios, A. F.: The oceanic sink for anthropogenic CO<sub>2</sub>, *Nature*, 305, 367–371, DOI: 10.1126/science.1097403, 2004.
- Schlitzer, R., Anderson, R. F., Masferrer Dodas, E., et al.: The GEOTRACES Intermediate Data Product 2017, *Chem. Geol.* 493, 210–223, <https://doi.org/10.1016/j.chemgeo.2018.05.040>, 2018.
- Smethie, W. M. Jr., and Swift, J. H.: The tritium-Krypton-85 age of Denmark Strait Overflow Water and Gibbs Fracture Zone Water just 805 south of Denmark Strait, *J. Geophys. Res.: Oceans*, 94, 8265–8275, <https://doi.org/10.1029/JC094iC06p08265>, 1989.
- Steinfeldt, R., and Rhein, M.: Spreading velocities and dilution of North Atlantic Deep Water in the tropical Atlantic based on CFC time series, *J. Geophys. Res.: Oceans*, 109(C3), C03046, <https://doi.org/10.1029/2003JC002050>, 2004.
- Steinfeldt, R., Rhein, M., and Walter, M.: NADW transformation at the western boundary between 66°W/20°N and 10°N, *Deep-Sea Res. I*, 54(6), 835–855, <https://doi.org/10.1016/j.dsr.2007.03.004>, 2007.
- 810 Steinfeldt, R., Rhein, M., Bullister, J. L., and Tanhua, T.: Inventory changes in anthropogenic carbon from 1997–2003 in the Atlantic Ocean between 20°S and 65°N, *Global Biogeochem. Cycles*, 23, GB3010, <https://doi.org/10.1029/2008GB003311>, 2009.



- Stendardo, I., Kieke, D., Rhein, M., Gruber, N., and Steinfeldt, R.: Interannual to decadal oxygen variability in the mid-depth water masses of the eastern North Atlantic, *Deep-Sea Res. I*, 95(1), 85–98, <https://doi.org/10.1016/j.dsr.2014.10.009>, 2015.
- 815 Stramma, L., Kieke, D., Rhein, M., Schott, F., Yashayaev, I., and Koltermann, K. P.: Deep Water changes at the western boundary of the subpolar North Atlantic during 1996 to 2001, *Deep-Sea Res. I*, 51(8), 1033–1056, <https://doi.org/10.1016/j.dsr.2004.04.001>, 2004.
- Swift, J. H., Aagaard, D., and Malmberg, S. V.: The contribution of the Denmark Strait Overflow to the deep North Atlantic, *Deep Sea Res.*, 27, 29–42, [https://doi.org/10.1016/0198-0149\(80\)90070-9](https://doi.org/10.1016/0198-0149(80)90070-9), 1980.
- Sy, A., Rhein, M., Lazier, J. R. N., Koltermann, K. P., Meincke, J., Putzka, A., and Bersch, M.: Surprisingly rapid spreading of newly formed intermediate waters across the North Atlantic Ocean, *Nature*, 386, 675–679, 1997.
- 820 Talley, L. D.: Some aspects of ocean heat transport by the shallow, intermediate and deep overturning circulations, in: *Mechanisms of Global Climate Change at Millennial Time Scales* (eds P.U. Clark, R.S. Webb and L.D. Keigwin), ISBN: 9781118664742, <https://doi.org/10.1029/GM112p0001>, 1999.
- Tanhua, T., Bulsiewicz, K., and Rhein, M.: Spreading of Overflow Water from the Greenland to the Labrador Sea, *Geophys. Res. Lett.*, 32(10), L10605, <https://doi.org/10.1029/2005GL022700>, 2005.
- 825 Tanhua, T., Waugh, D. W., and Wallace, D. W. R.: Use of SF<sub>6</sub> to estimate anthropogenic CO<sub>2</sub> in the upper ocean, *J. Geophys. Res.: Oceans*, 113, C04037, <https://doi.org/10.1029/2007JC004416>, 2008.
- Tanhua, T., Hoppema, M., Jones, E. M., Stöven, T., Hauck, J., Dávila, M. G., Santana-Casiano, M., Álvarez, M., and Strass, V. H.: Temporal changes in ventilation and the carbonate system in the Atlantic sector of the Southern Ocean, *Deep-Sea Res. II*, 138, 26–38, <https://dx.doi.org/10.1016/j.dsr2.2016.10.004>, 2017.
- 830 Terenzi, F., Hall, T. M., Khatiwala, S., Rodehacke, C. B., and LeBel, D. A.: Uptake of natural and anthropogenic carbon by the Labrador Sea, *Geophys. Res. Lett.*, 34, L06608, <https://doi.org/10.1029/2006GL028543>, 2007.
- van Heuven, S. M. A. C., Hoppema, M., Huhn, O., Slagter, H. A., and de Baar, H. J. W.: Direct observation of increasing CO<sub>2</sub> in the Weddell Gyre along the Prime Meridian during 1973–2008, *Deep-Sea Res. II*, 58(25–26), 2613–2635, <https://doi.org/10.1016/j.dsr2.2011.08.007>, 2011.
- 835 Vázquez-Rodríguez, M., Touratier, F., Lo Monaco, C., Waugh, D. W., Padin, X. A., Bellerby, R. G. J., Goyet, C., Metzl, N., Ríos, A. F., and Pérez, F. F.: Anthropogenic carbon distributions in the Atlantic Ocean: data-based estimates from the Arctic to the Antarctic, *Biogeosciences*, 6, 439–451, <https://doi.org/10.5194/bg-6-439-2009>, 2009.
- Våge, K., Pickart, R. S., Thierry, V., Reverdin, G., Lee, C. M., Petrie, B., Agnew, T. A., Wong, A., and Ribergaard, H. M.: Surprising return of deep convection to the subpolar North Atlantic Ocean in winter 2007–2008, *Nature Geoscience*, 2, 67–72, <https://doi.org/10.1038/ngeo382>, 2009.
- 840 Wanninkhof, R., Doney, S. C., Bullister, J. L., Levine, N. M., Warner, M., and Gruber, N.: Detecting anthropogenic CO<sub>2</sub> changes in the interior Atlantic Ocean between 1989 and 2005, *J. Geophys. Res.: Oceans*, 115, C11028, <https://doi.org/10.1029/2010JC006251>, 2010.
- Watson, A. J., Messias, M. J., Fogelqvist, E., Van Scoy, K. A., Johannessen, T., Oliver, K. I. C., Stevens, D. P., Rey, F., Tanhua, T., and Olsson, K. A.: Mixing and convection in the Greenland Sea from a tracer-release experiment, *Nature*, 401(6756), 902–904, <https://doi.org/10.1038/44807>, 1999.
- 845 Waugh, D. W., Haine, T. W. N., and Hall, T. M.: Transport times and anthropogenic carbon in the subpolar North Atlantic Ocean, *Deep-Sea Res. I*, 51, 1475–1491, <https://doi.org/10.1016/j.dsr.2004.06.011>, 2004.
- Waugh, D. W., Hall, T. M., McNeil, I., Key, R., and Matear, R. J.: Anthropogenic CO<sub>2</sub> in the oceans estimated using transit time distributions, *Tellus*, 58B(5), 376–389, [doi:10.1111/j.1600-0889.2006.00222.x](https://doi.org/10.1111/j.1600-0889.2006.00222.x), 2006.



- 850 Waugh, D. W., Primeau, F., DeVries, T., and Holzer, M.: Recent Changes in the Ventilation of the Southern Oceans, *Science*, 339, 568–570, doi:10.1126/science.1225411, 2013.
- Woosley, R. J., F. J. Millero, and Wanninkhof, R.: Rapid anthropogenic changes in CO<sub>2</sub> and pH in the Atlantic Ocean: 2003–2014, *Global Biogeochem. Cy.*, 30, 70–90, <https://doi.org/10.1002/2015GB005248>, 2016.
- Yashayaev, I.: Hydrographic changes in the Labrador Sea, 1960–2005, *Prog. Oceanogr.*, 73, 242–276, 855 <https://doi.org/10.1016/j.pocean.2007.04.015>, 2007.
- Yashayaev, I., van Aken, H. M., Holliday, N. P., and Bersch, M.: Transformation of the Labrador Sea Water in the subpolar North Atlantic, *Geophys. Res. Lett.*, 34, L22605, <https://doi.org/10.1029/2007GL031812>, 2007.
- Yashayaev, I., and Loder, J. W.: Recurrent replenishment of Labrador Sea Water and associated decadal-scale variability, *J. Geophys. Res.: Oceans*, 121, 8095–8114, <https://doi.org/10.1002/2016JC012046>, 2016.



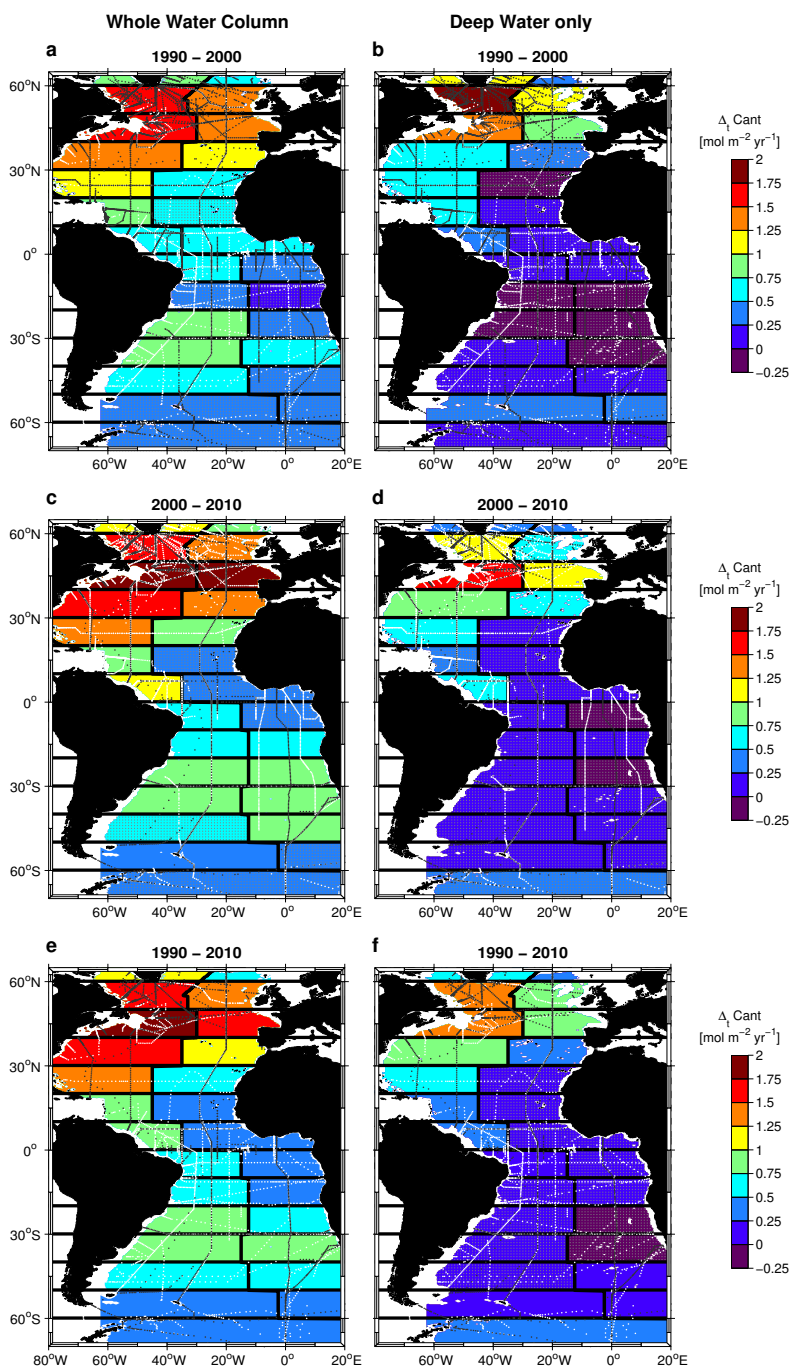


**Figure 8.** Mean  $C_{\text{ant}}$  storage rate ( $\Delta_i C_{\text{ant}}$ ) for the decades between 1990 and 2010 based on decadal data. Left column: whole water column, right column: only deep and bottom water masses. Top row: 1990–2000, middle: 2000–2010, bottom: 1990–2010. Only areas with a water depth larger than 200m are considered. Station locations for the first period (1982–1994 in a, b, e, f and 1995–2005 in c, d) are marked in white, those for the second period (1995–2005 in a, b and 2006–2014 in c, d, e, f) in grey. Regions with differences smaller than the error range are stippled.

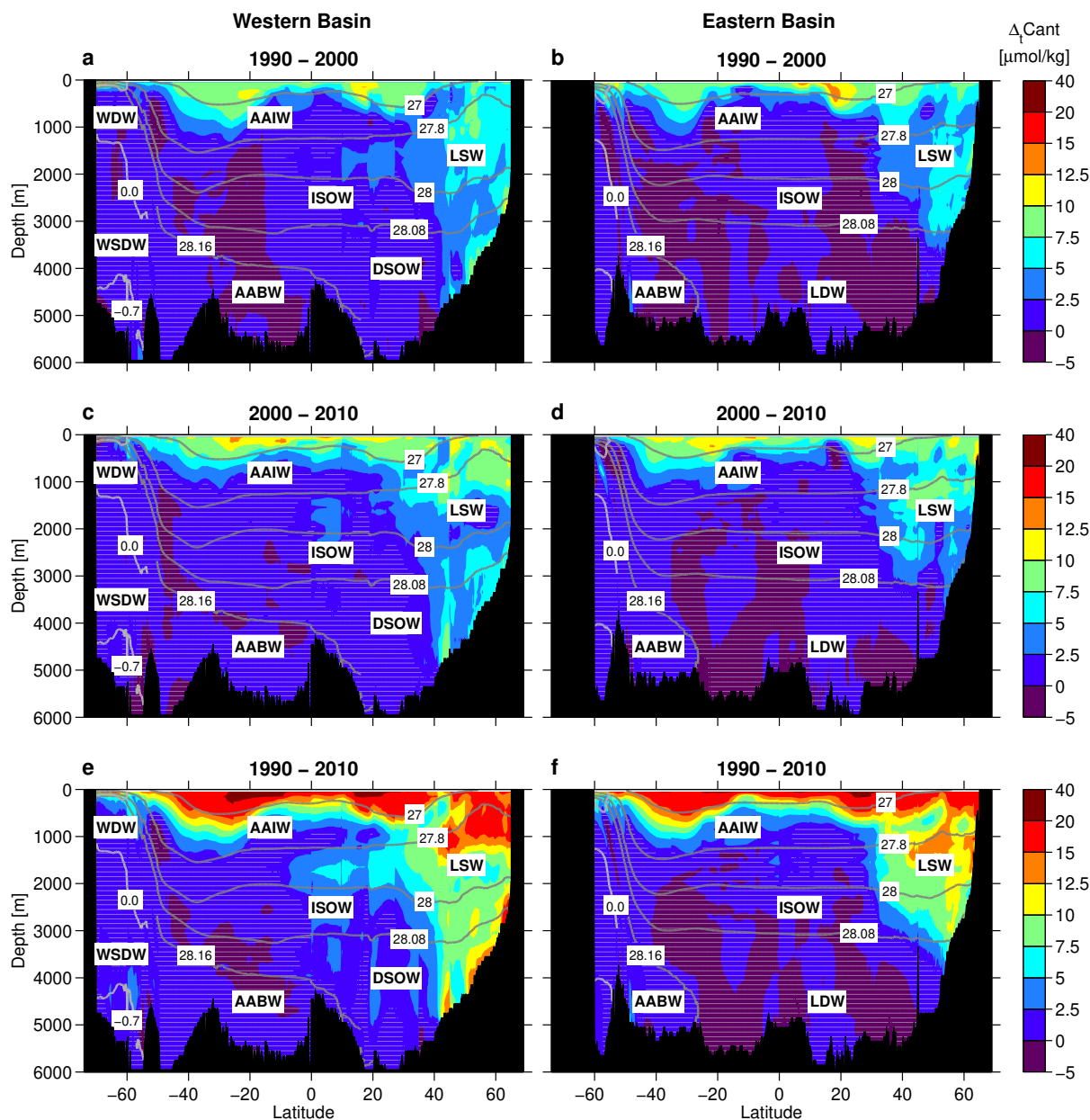


**Figure 9.** Zonal mean sections of  $C_{ant}$  concentration changes ( $\Delta_t C_{ant}$ ) based on decadal data for the periods between 1990 and 2010. Left column: western basin; right column: eastern basin; top row: 1990–2000, middle: 2000–2010, bottom: 1990–2010. Regions with differences smaller than the error range are stippled. Contour lines are shown as in Fig. 2.

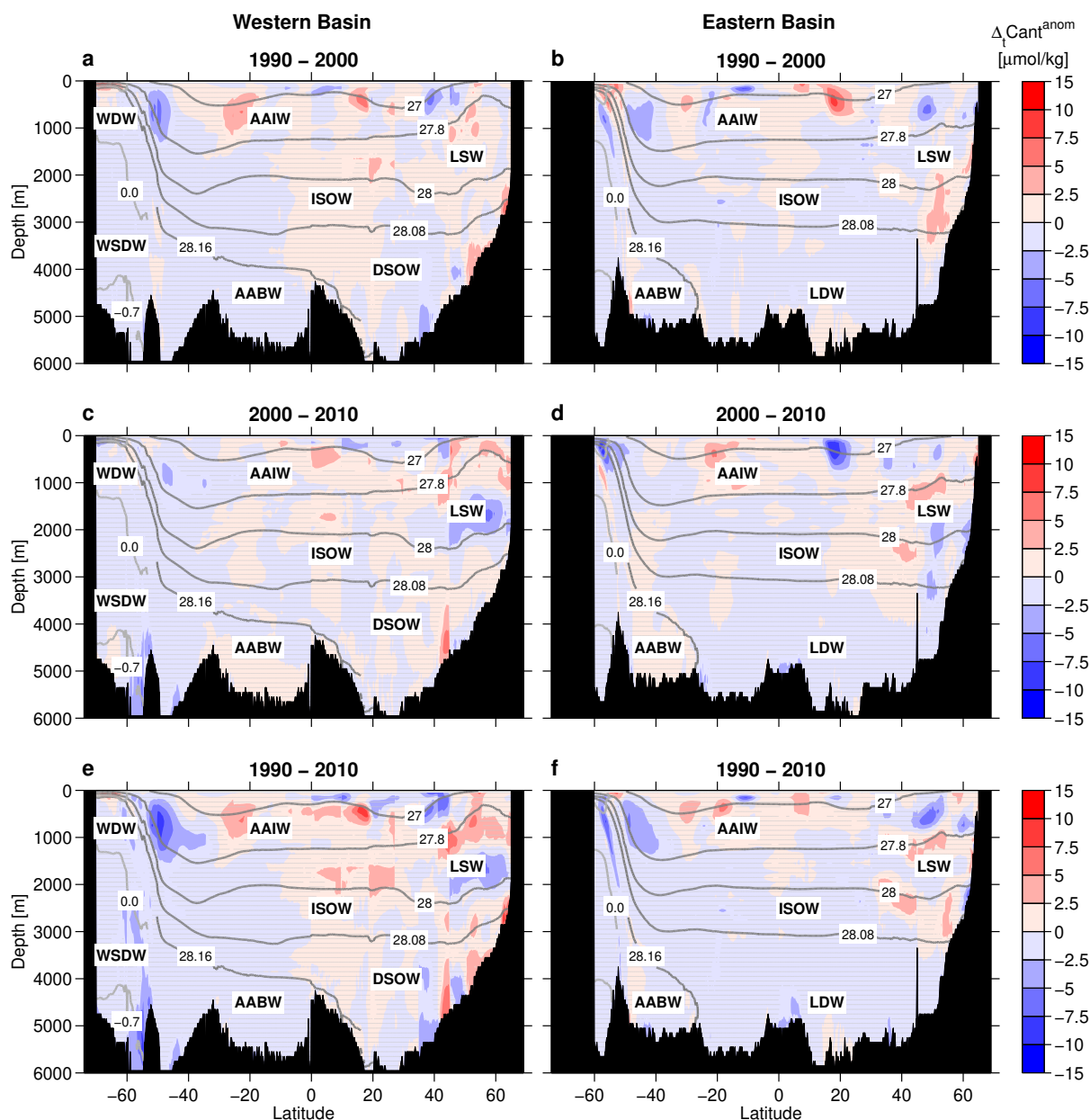


**Figure 10.** Zonal mean sections of  $\Delta_t C_{\text{ant}}^{\text{anom}}$  ( $C_{\text{ant}}$  forecast based on tracer data from the first period minus  $C_{\text{ant}}$  based on tracer data from the second period). Left column: western basin, right column: eastern basin; top row: 1990–2000, middle: 2000–2010, bottom: 1990–2010. Regions with differences smaller than the error range are stippled. Contour lines are shown as in Fig. 2.

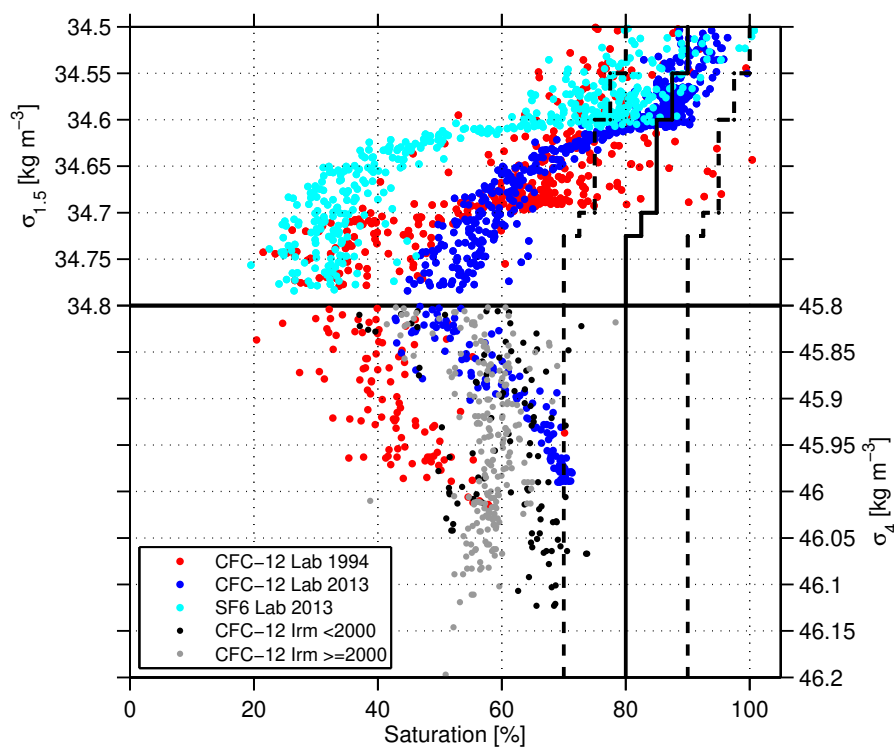


**Figure B1.** CFC-12 and SF<sub>6</sub> data below 500 m from the Labrador Sea (years 1994 and 2013) and the Irminger Sea (years prior to and after 2000), expressed as saturation with respect to the actual solubility equilibrium. Also shown is the assumed tracer saturation and the error margin of  $\pm 10\%$ .

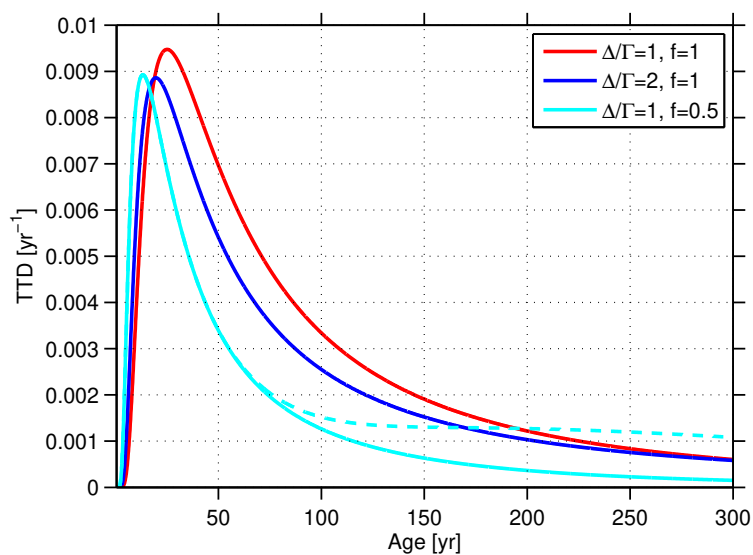


**Figure C1.** TTDs derived from an observed CFC-12 concentration of  $0.5 \text{ pmol kg}^{-1}$  in 2010, a CFC-saturation of 0.85, a potential temperature of  $\theta = 3^\circ\text{C}$ , and a salinity of  $S = 34.9$ . Shown are TTDs for  $f = 1$  and  $\Delta/\Gamma = 1$  and  $\Delta/\Gamma = 2$  respectively, as well as for  $f = 0.5$  and  $\Delta/\Gamma = 1$ . For the latter case, also an assumed old TTD with with  $\Gamma = 500 \text{ yr}$  and  $\Delta = 250 \text{ yr}$  is added (dashed cyan line).

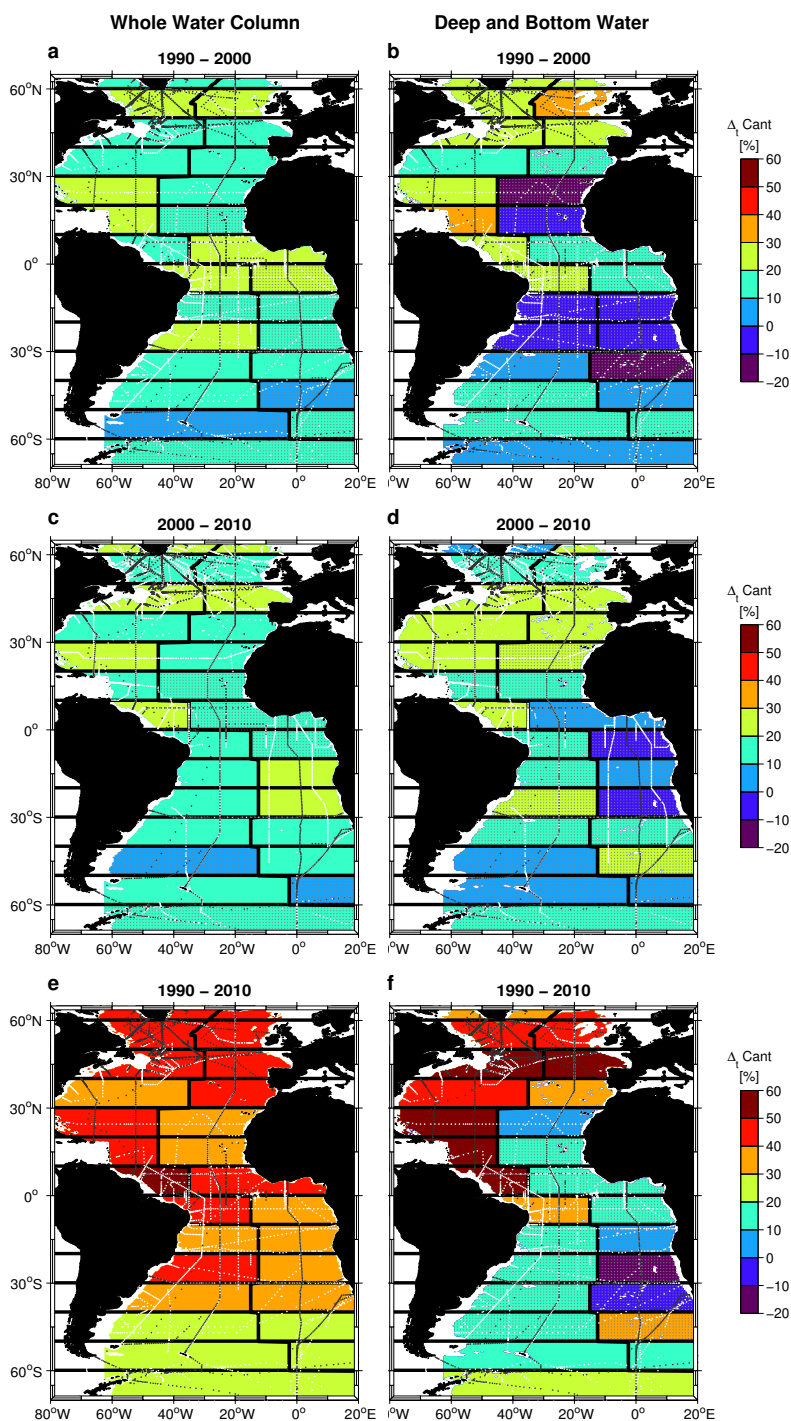


**Figure D1.** Left column: whole water column, right column: only deep and bottom water masses. Top row: 1990–2000, middle: 2000–2010, bottom: 1990–2010. Only areas with a water depth larger than 200 m are considered. Station locations for the first period (1982–1994 in a, b, e, f and 1995–2005 in c, d) are marked in white, those for the second period (1995–2005 in a, b and 2006–2014 in c, d, e, f) in grey. Regions with differences smaller than the error range are stippled.